Collective epithelial migration drives timely morphogenesis of the retinal neuroepithelium

Jaydeep Sidhaye[1,2], Niklas Iffländer[1] and Caren Norden[1]*

[1] Max Planck Institute of Molecular Cell Biology and Genetics, Pfotenhauerstraße 108, 01307 Dresden, Germany

[2] DIGS-BB, Technische Universität Dresden, Pfotenhauer Str. 108, 01307 Dresden, Germany

* Corresponding Author: Caren Norden
MPI-CBG
Pfotenhauerstraße 108
01307 Dresden
Germany
Phone: +49 351 210-2802
Fax: +49 351 210-1489
Email: norden@mpi-cbg.de

Summary

Organ formation is a complex, multi-scale event involving changes at the intracellular, cellular and tissue level. A key step in organogenesis is the formation of characteristically shaped organ precursors. However, the cellular mechanisms driving organ precursor formation are not well understood. Here, we investigate the epithelial rearrangements responsible for the development of the hemispherical retinal neuroepithelium (RNE), a part of the optic cup. We show that, surprisingly, active collective epithelial migration of cells at the rim of the cup is the most prominent player in RNE formation. This rim involution is driven by progressive cell-matrix contacts and actively translocates prospective RNE cells to their correct location before they adopt neuroepithelial fate. Failure of rim migration during neuroepithelium formation leads to ectopic determination of RNE cells and consequently impairs eye formation. Overall, this study illustrates how spatiotemporal coordination between morphogenic movements and fate determination critically influences organogenesis.

Introduction

In many developmental contexts, organ formation includes rearrangements of epithelial sheets. Such rearrangements then give rise to organ precursors that later develop into mature organs. For example, epithelial rearrangements that form the imaginal discs of *Drosophila* larvae generate fly organs including wings and legs (Morata, 2001). Similarly, the vertebrate neural tube is shaped by epithelial reorganization and later develops into the brain and spinal cord (Greene and Copp, 2014). Epithelial reorganization occurs via changes in the morphology, number and location of cells, and ultimately defines the architecture of the developing organ (Lecuit and Le Goff, 2007). When epithelial reorganization and subsequent organ precursor architecture are impaired, the structure and function of the mature organ can be compromised. For instance, defects in cell-matrix adhesion resulting in impaired wing imaginal disc formation ultimately cause a blistered wing (Dominguez-Gimenez et al., 2007). Similarly, defects in epithelial fusion of neural folds can lead to problems in neural tube closure and generate severe birth defects in mammals (Greene and Copp, 2014). Hence, deciphering how epithelial morphogenesis shapes organ precursors is crucial to understanding organ development.

One outstanding model to investigate how epithelial biology shapes organ architecture is the developing vertebrate retina. Here, the retinal neuroepithelium (RNE) represents the organ precursor that later gives rise to all neurons of the mature retina (Fuhrmann, 2010). The hemispheric RNE located in the optic cup develops from the bilayered optic vesicle (Bazin-Lopez et al., 2015), and its formation involves complex epithelial rearrangements including tissue elongation, sheet invagination and epithelial sheet movements (Martinez-Morales et al., 2009; Heermann et al., 2015; Kwan et al., 2011). It has been shown in mouse and human retinal organoid *ex vivo* cultures that the optic vesicle epithelium self-organizes into a hemispherical shape due to high proliferation in a

confined space (Eiraku et al., 2011; Nakano et al., 2012). However, work in zebrafish and *Xenopus* shows that RNE development continues even when cell proliferation is blocked (Harris and Hartenstein, 1991; Kwan et al., 2011). Such differences highlight the importance of *in vivo* studies of optic cup formation in addressing how the RNE is formed during embryonic development.

Due to its unmatched imaging potential, the zebrafish is an excellent model to understand *in vivo* optic cup formation at both the cellular and the tissue level. Work in zebrafish and medaka led to the assumption that basal constriction of RNE cells is the main driver of RNE invagination (brown cell, Figure 1A) (Martinez-Morales et al., 2009; Bogdanović et al., 2012). However, it remains unclear whether basal constrictions alone can drive RNE morphogenesis. Importantly, it is also known that a significant number of cells concomitantly move into the optic cup by rim involution (blue cell, Figure 1A) (Kwan et al., 2011; Picker et al., 2009; Heermann et al., 2015). To date, however, it remains unclear whether rim involution is actively involved in RNE morphogenesis, and if so, which molecular mechanisms are responsible for driving it.

Here, we use a multi-scale approach to investigate the epithelial rearrangements occurring during RNE formation at the single-cell and the tissue level. We find that RNE morphogenesis in zebrafish crucially depends on rim involution. Rim cells migrate actively at the single-cell level but show characteristics of collective epithelial migration at the tissue level. When rim migration is perturbed, not all prospective neuroepithelial cells reach the RNE. This results in severely disturbed retinal architecture. Thus, collective epithelial migration of rim cells coordinates the timely integration of future neuroepithelial cells into the hemispherical RNE and is essential to prevent cells from adopting neuroepithelial fate at ectopic locations.

Results

Invagination of the retinal neuroepithelium involves basal cell surface reduction and basal accumulation of contractile actomyosin

To begin to elucidate the mechanisms of RNE formation, we focused on central RNE invagination. It has been hypothesized that central RNE invagination depends on basal constriction of central neuroepithelial cells (Figure 1A, brown cell) (Martinez-Morales et al., 2009). To test this idea, we labeled the cell cortex at different stages of optic cup morphogenesis from 15 somite stage (ss) to 28 ss (16 hours post fertilization (hpf) to 24 hpf) using the F-actin marker phalloidin. We measured the average cell density at the base of the RNE. We noted that basal cell density increased significantly during optic cup invagination (Figure S1A and S1C). Concomitantly, the average basal area (basal footprint) of RNE cells was reduced by about 45%. This reduction mainly occurred during the first half of the invagination process between 15 ss and 21 ss (Figure 1B). In contrast, the average apical area of cells increased during this phase. As a result, the average apical area was larger than the average basal area at the end of the process. This indicates that cells undergo overall shape changes during invagination that result in cones with a narrower basal surface (Figure 1B).

To determine whether the observed reduction in basal area was linked to changes in actomyosin distribution, we imaged actin and myosin distribution during RNE morphogenesis. At the onset of neuroepithelial invagination, the actin marker GFP-UtrophinCH (Norden et al., 2009) accumulated at the basal side of the RNE (Figure 1C) similarly to the myosin marker, myl12.1-EGFP (Norden et al., 2009) (Figure 1D). Basal actin and myosin enrichment was specific to the invaginating zone of the neuroepithelium and was not observed in other regions of the optic cup (Figure 1C, 1D). These findings were corroborated by phalloidin (actin) and anti-phosphomyosin (active myosin) staining of samples fixed between 15 ss and 30 ss (Figure 1E, 1G and S1B).

Quantitative analysis of phalloidin and phosphomyosin intensity distribution along the apicobasal axis of the neuroepithelium showed that the basal actomyosin bias spanned about 15% of the RNE height (Figure 1F and 1H). Thus, invagination of the neuroepithelium is accompanied by basal foot shrinkage and basal accumulation of contractile actomyosin.

Inhibition of basal actomyosin contraction delays but does not prevent RNE invagination

To test whether the pool of contractile basal actomyosin is involved in RNE invagination, we perturbed myosin contractility using the drug Rockout, which is known to inhibit the Rock pathway upstream of actomyosin activity (Yarrow et al., 2005). Upon 7 h of Rockout treatment, lens structures in treated embryos developed similarly to controls (Figure 2A). In contrast, the basal actomyosin bias in central RNE cells was markedly reduced (Figure 2A, 2C and 2D). Despite this reduction of actin and myosin however, the invagination angle (defined as the angle between the inner lips of the optic cup and the center of the RNE, see schematic in Figure 2F and Material and Methods) was only moderately wider with an average of 80° (SEM ± 3.979 n=15) compared to 60° (SEM ± 2.631 n=14) in controls (Figure 2F). Thus, although RNE invagination was not as efficient in the treated embryos as in controls, it was nevertheless initiated (Figure 2A and 2J). While 40% of embryos showed an accumulation of cells at the rim of the cup after 7 h Rockout treatment (n=30 embryos per experiment, N=4 experiments; Figure 2A and 2B), the proportion of embryos with this phenotype was reduced to 25% after 10 to 12 hours of drug treatment and in 50% of embryos the optic cups developed comparable to controls (Figure 2B) (n=30 embryos N=4 experiments; 25% embryos showed severe developmental delay or death). To better understand the progression of RNE formation in the Rockout condition, we performed live imaging of GFP-UtrophinCH in Rockout-

treated embryos. This confirmed that RNE invagination still took place albeit with slower kinetics even when basal actin levels were greatly reduced (Figure 2E and 2G). Interestingly, at 30ss, the end point of optic cup invagination, the basal foot area was similar in controls and Rockout-treated embryos (Figure 2G). This observation suggests that basal surface shrinkage does not depend solely on basal actomyosin contractility and that it can be compensated by other mechanisms.

RNE morphogenesis persists in the absence of cell proliferation

Basal foot shrinkage could also result from cell compaction when an increasing number of cells inhabit the RNE. One way to increase cell numbers is proliferation, and it has been shown that RNE formation is accompanied by high proliferation rates (Kwan et al., 2011). In addition, proliferation has been suggested as a driving force for optic cup formation *in vitro* (Eiraku et al., 2011). In zebrafish, however, optic cup invagination persists even when proliferation is inhibited (Kwan et al., 2011). To test whether tissue compaction caused by ongoing proliferation can influence RNE invagination, we inhibited proliferation with hydroxyurea and aphidicolin from 10 ss onwards (Kwan et al., 2011), leading to markedly reduced pH3 staining compared to controls (Figure S2A). Consequently, the neuroepithelium hosted fewer cells and these cells adopted a more columnar morphology than control cells (Figure S2B and S2C). Furthermore, following inhibition of proliferation, cells in the RNE displayed a slightly larger average basal footprint than control cells (Figure 2G). Despite this, optic cup formation still occurred and invagination angles were not severely affected (Figure 2F and S2B). This shows that RNE invagination can take place when compaction due to cell proliferation is compromised and leads to RNE cells with a broader basal footprint (Figure 2G). However, this suggests that additional processes participate in RNE morphogenesis.

RNE morphogenesis involves active cell migration at the rim of the optic cup

One process that occurs concomitantly with RNE invagination is rim cell involution. This phenomenon is most prominent at the ventral and temporal side of the cup and relocates a substantial number of cells into the RNE, which may result in increased compaction (blue cell, Figure 1A) (Kwan et al., 2011; Heermann et al., 2015; Picker et al., 2009). As we noted that rim cells in the Rockout-treated embryos continued to move into the cup (Figure 2E), we wondered whether these cell movements could explain the recovery of RNE morphogenesis defects upon Rockout treatment. We thus asked if rim involution was actively involved in shaping the RNE. To initially understand how cells move at the rim, we characterized their single-cell dynamics. Mosaic labeling of rim cells with the membrane marker mKate2-ras and the apical marker Par3-GFP revealed that moving rim cells kept a stable apical domain but were very dynamic at the basal side (Figure 3A). As microtubules marked with EMTB-tdTomato did not show significant reorganization during rim involution, we concluded that microtubules were not majorly involved in the cellular dynamics (Figure S3A). Instead, we observed that cells extended dynamic lamellipodia-like protrusions in the direction of movement (Figure 3A). These protrusions were actin rich, as shown by GFP-UtrophinCH localization (Figure 3B), underlining their lamellipodial character. Such lamellipodia were only observed in the rim cells and were not seen in cells of the central RNE (Figure 3B). When we quantified protrusive activity during rim migration, we found that the vast majority of protrusions occurred in the direction of movement, the leading side of the cells facing the invaginating zone (Figure 3C). This showed that the protrusive activity of rim cells is directional. Interestingly, actin-rich lamellipodia formation and rim migration were still observed in the Rockout condition (Figure 3D), further indicating that the migratory behaviour of rim cells occurs independently of the basal actomyosin bias in the central RNE cells.

Once rim cells reached the RNE, basal actin dynamics changed considerably. Lamellipodia formation ceased and a stable pool of basal actin was observed similar to the actin distribution in the central RNE cells (Figure 3B). Likewise, while myosin labeled by DD-MRLC-GFP occurred as dynamic spots at the basal side of cells during rim movement (Figure S3B), it became stably enriched once the cells reached the inner side of the optic cup. Together, these data show that rim cells exhibit dynamic and directional basal lamellipodia formation that coincides with directed migratory behaviour. Once cells reach the RNE, however, they change their basal dynamics and establish a stable basal actomyosin pool similar to the central RNE cells.

Rim involution involves active collective cell migration

Our analysis so far indicated that rim cells move by active migration at the single-cell level. However, the lack of changes in the apical domain indicated that these cells remained integrated within the epithelial sheet (Figure 3A and 3B), arguing that the rim cells migrate collectively. To test this idea, we mosaically expressed a dominant-negative Rac (DN-Rac, Rac1-T17N) construct (Subauste et al., 2000) under a heat shock promoter for temporal control (Norden et al., 2009; Strzyz et al., 2015). To evaluate the efficiency of the construct expression, we assessed its effects on the actin cytoskeleton in different cell types. We noted that actin arrangements were altered in both retinal neuroepithelial cells and epidermal cells (Figure S3C). Thus, we concluded that the construct was functional and allowed us to interfere with lamellipodia formation in only a subset of cells to observe how this influences single cell and epithelial dynamics. DN-Rac-expressing cells exhibited abnormal morphology and showed the expected phenotypes. Instead of forming lamellipodia, cells displayed random membrane protrusive activity more reminiscent of very long filopodia as noted before in this condition (Lodyga et al., 2010)(Figure 3F). However, these undirected protrusions

did not reconstitute lamellipodia-dependent cell motility and cells did not form the dynamic basal activity seen in control rim cells (Figure 3F). Nevertheless, live imaging showed that in spite of the abnormal morphology and impaired dynamics the mosaic DN-Rac-expressing cells moved into the same direction as the surrounding control cells and reached the RNE with their unperturbed neighbors. However, migration speed was reduced (Figure 3E) and the efficiency of rim involution was correlated with the number of cells affected by DN-Rac (Figure 3F). This data suggests that the DN-Rac expressing rim cells that show migratory defects at the single-cell level can still undergo rim involution with help of neighboring cells. Therefore, we conclude that rim cell movement is a mode of collective epithelial cell migration.

Rim cell migration depends on dynamic cell-ECM adhesion

We next asked how exactly lamellipodia formation can drive rim cell movement. Lamellipodia-driven migration depends on dynamic attachments of cells to the surrounding extracellular matrix (ECM) (Friedl and Wolf, 2010). Thus, we assessed the distribution of ECM during rim movement by immunostainings for the ECM components Laminin, Chondroitin sulfate and Fibronectin. These ECM components were only weakly expressed beneath the developing retinal pigment epithelium (RPE), but showed stronger accumulation in the rim zone, the developing lens placode and the invaginating RNE (Figure S3A and S3B). Hence, we speculated that the migrating rim cells use their lamellipodia to dynamically attach to the underlying ECM and thereby generate force for movement. Imaging of the focal adhesion markers Integrin-β1-mKate2 and Paxillin-mKate2 markers indeed revealed short-lived foci appearing and disappearing from the basal side of rim cells during live imaging (Figure 4A and 4B). Thus, rim cells make and break cell-matrix contacts during their movement. However, once cells reach the RNE, stable integrin and paxillin adhesions were formed as seen for the actin marker and cells

stopped their active migration behavior (Figure 4A and 4B). Co-imaging of the localization dynamics of Paxillin-mKate2 and GFP-UtrophinCH corroborated this finding. While the cells in the rim zone lacked basal enrichment of actin and paxillin, cells of the central RNE showed stable basal enrichment of Paxillin coinciding with the basal accumulation of actin (Figure S4C). This suggested that the active migration mode observed for rim cells is confined to the zone that connects the developing RPE to the RNE, where cells move from one epithelial layer into the other by turning 180°**.** Once the cells reach the inner layer of the cup they change from active adhesion remodeling to stable cell-ECM attachment.

To verify that active remodeling of focal adhesions and ECM is indeed necessary for successful rim cell migration, we perturbed cell-matrix attachment by interfering with the ECM or the intracellular attachment side. To this end, we knocked down laminin α-1 and ojoplano/opo using previously published morpholinos (Randlett et al., 2011; Martinez-Morales et al., 2009) (see Figure S5A-S5D for controls for efficiency of morpholino knockdown by immunostaining and Western blot). Laminin α-1 depletion interferes directly with ECM integrity and it has been shown to be involved at different stages of optic cup development (Ivanovitch et al., 2013; Bryan et al., 2016). opo is a regulator of endocytosis that acts via integrins and has been shown to play an important role in eye morphogenesis (Martinez-Morales et al., 2009; Bogdanović et al., 2012). Its activity is linked to expression of the early RNE transcription factor Vsx2 (Kimura et al., 2006) meaning that it becomes active during RNE formation (Gago-Rodrigues et al., 2015). Morpholino knockdown of either gene led to impaired optic cup formation at 30 ss. In both conditions, epithelial tissue accumulated at the temporal side of the optic cup, giving the cup an S-shaped appearance instead of the C-shaped appearance seen in controls (Figure 4C and 4D). Defects were more severe in the laminin knock down

condition than in the opo morphants. Live imaging of both conditions confirmed that the S-shaped phenotype was related to impaired rim cell migration, as the speed of rim cells was reduced (Figure 3E, 4E, 4F). This reduced speed may be explained by the inability of migrating cells to make efficient lamellipodia contact with the underlying matrix. We further noticed that basal actomyosin accumulation was reduced in both laminin and opo knockdown conditions (Figure 4D, S5E, S5F). Accordingly, invagination angles were severely affected (Figure 2F), arguing that a combination of impaired rim migration and actin-driven central cell invagination led to the extreme phenotypes observed.

Together, these data imply that interference with cell-ECM attachment leads to disturbance of the two epithelia involved in hemispheric RNE formation, rim cells cannot actively migrate due to impaired of cell ECM-attachments and central cells failed establish the basal actomyosin bias.

Bleb induction affects rim cell migration and leads to impaired RNE architecture

To elucidate the cellular changes that led to the impaired rim cell migration upon interference with cell-ECM attachment, we analyzed the basal membrane dynamics of rim cells in the laminin and opo knockdown conditions. We noted that the rim cells in the morphants exhibited basal bleb-like protrusions instead of the lamellipodia observed in control embryos. These blebs contained actin but were devoid of myosin (Figure 4G and 4H). The finding that the cells that failed to undergo active rim migration exhibited blebs instead of lamellipodia made us ask whether enforced bleb induction itself could interfere with rim cell migration. To test this idea, we knocked down the ERM protein family member Ezrin using a published morpholino (Link, 2006). Ezrin is a protein that links actin and the plasma membrane and its knockdown has been shown to lead to increased blebbing and reduced migration rates of zebrafish prechordal plate precursor cells (Schepis et al., 2012) (see Figure S5G and S5H for controls for efficiency of

morpholino knockdown by immunostaining and Western blot and overall morphant morphology). During RNE formation, we observed that ezrin knockdown specifically induced basal blebbing in the rim cell area, whereas lateral sides of the rim cells and central RNE cells were not affected (Figure 5A). This specificity of bleb induction may be explained by weakening of the basal cortex due to normal lamellipodia formation with a consequent enhancement of the effect of ezrin depletion at this location. Ezrin depletion resulted in a phenotype similar to Laminin or Integrin interference and rim cells did not reach the central RNE (Figure 5B and 5C). Average cell speed was reduced by 27% (Figure 4E, 5F). Importantly, however, we only observed a minor effect on basal actomyosin accumulation in the RNE (Figure 5D and 5E). Overall, while formation of the lens and the RPE occurred similar to the control situation (Figure 5C), RNE morphogenesis in ezrin morphants was defective and at 30 ss an S-shaped optic cup was observed (Figure 5B and 5C). This phenotype did not recover upon continued development (Figure 5B). In contrast, the cells that stayed outside the optic cup eventually made stable instead of dynamic contact to the surrounding ECM outside the central RNE, as shown by Paxillin localization (Figure 5G and 5H). Cells thereby attained neuroepithelial-like morphology. We conclude that ECM attachment in rim cells is important for lamellipodia formation and successful rim cell migration. When cell-ECM attachment is perturbed, rim cells form blebs instead of lamellipodia but these blebs cannot rescue cellular movement. Consequently, upon bleb induction cells are left outside the neuroepithelium where they take on neuroepithelial morphology at ectopic positions.

Rim cell migration ensures timely entry of RNE cells into the optic cup

As interference with rim movement led to an accumulation of cells outside the RNE, and these cells eventually adopted RNE-like morphology, we asked whether they would also

adopt RNE fate. To test this, we used Vsx2, an early retinal transcription factor specific for RNE fate (Kimura et al., 2006). Live imaging of the transgenic line Tg(*vsx2*::GFP) expressing GFP under the *vsx2* promoter allowed us to follow RNE specification. In control embryos, GFP was primarily expressed in the invaginating RNE layer and the signal was weak in cells of the rim zone. Only when rim cells reached the inner RNE did they express GFP more prominently (Figure 6A). However, in the ezrin knockdown condition, rim cells that accumulated outside the RNE expressed GFP ectopically at this location (Figure 6A and 6B). Such ectopic expression of *vsx2* outside the optic cup was also observed in laminin and opo morphants. Also here cells failed to migrate and an S-shaped cup was formed (Figure 6B). Thus, *vsx2* expression and RNE fate while seemingly temporally controlled were independent of correct cell position. In some ezrin morphants, these displaced RNE cells initiated a second invagination zone and even a secondary lens-like structure (Figure 6C). These phenotypes persisted until 36hpf, when neurogenesis in the RNE is known to start (Weber et al., 2014), resulting in abnormal architecture of the optic cup (Figure 6D). Our results thus suggest that rim migration functions as a mechanism to ensure that initially 'misplaced' prospective RNE cells are moved to their correct location before they adopt RNE fate, making it a crucial step for all further retinal development.

Discussion

In this study we show that active rim involution is the major driver of optic cup formation. While actomyosin-related basal foot shrinkage of central RNE cells seems to facilitate RNE invagination, it is the migration of rim cells into the RNE that is absolutely necessary to form the hemispheric RNE that gives rise to the future retina. Rim involution represents a novel mode of active collective epithelial migration that is essential to translocate prospective neuroepithelial cells into the invaginating RNE layer.

Thus, rim cell migration ensures the timely integration of prospective neuroepithelial cells into the optic cup, where they adopt retinal fate (summarized in Figure 7).

Rim cell migration and basal RNE cell shrinkage collectively contribute to efficient optic cup morphogenesis

The combination of RNE invagination and rim migration is the most efficient way to form the hemispherical RNE within a critical developmental timespan. However, while defects of central RNE basal foot shrinkage can be compensated over time by increased compaction due to an increasing number of inward-moving rim cells, impaired rim migration leads to failure of hemispheric RNE formation.

The interplay of epithelial rearrangements observed here includes both cell shape changes and migratory phenomena. Similar combinations of epithelial rearrangements are at play during other morphogenesis phenomena that occur in a rather short developmental time frame. For instance, during zebrafish posterior lateral line development, timely coordination between the epithelial rearrangements of microlumen formation and primordium migration determines the spacing of rosettes and in turn the lateral line architecture (Durdu et al., 2014). In contrast, in multiple other examples of epithelial bending phenomena including *Drosophila* mesoderm invagination (Leptin, 2005) or zebrafish midbrain-hindbrain boundary formation (Gutzman et al., 2008) cell shape changes are sufficient to drive morphogenesis. Thus, to understand dynamics of morphogenetic processes it is important to decipher how cell behaviors and eventually their relationship orchestrate tissue formation in many different contexts. This will be important for determining the common and diverse mechanisms underlying organ formation.

Distinct dynamics at the basal side of the epithelium drive RNE morphogenesis

Interestingly, all of the dynamic morphogenetic changes elucidated here occur at the basal side of the epithelium. In addition, depending on cell type and position, cell-ECM attachments can be modulated differentially in space and time to regulate distinct cell behaviors that shape organ development. In the rim region, basal cell dynamics are crucial for cell migration, whereas in the central region they assist the formation of stable basal adhesion and basal foot shrinkage. Basal domain dynamics are also involved in the formation of the zebrafish midbrain-hindbrain boundary, where the ECM is important for basal shrinkage of the boundary cells (Gutzman et al., 2008), and for the generation of the *Drosophila* follicular epithelium, where cell-ECM adhesion plays a crucial role in follicle rotation and egg elongation (Haigo and Bilder, 2011). However, most studies of established systems of epithelial morphogenesis such as gastrulation movements in *Drosophila* or vertebrate neurulation (Guillot and Lecuit, 2013) have focused on the dynamics of the apical domain. It will therefore be important to further explore the role of basal dynamics during morphogenesis in different developmental contexts.

Rim cells migrate collectively

We show that rim cells undergo active cell migration using dynamic lamellipodia and cell-ECM attachments while staying integrated within the epithelial sheet. Thus, rim cell migration is a previously uncharacterized form of collective epithelial cell migration. Collectiveness is demonstrated by our observation that when migration is impaired in a subset of cells, the surrounding control cells nevertheless move these migration-impaired cells into the invaginating RNE. This is reminiscent of a line dance like the Greek sirtaki, in which, even when a middle dancer stumbles, the rest of the line will pull him along in the direction of movement. As lately various morphogenetic phenomena have been discovered to include collective epithelial migration, including branching

morphogenesis of trachea in *Drosophila* and mammary gland development (Scarpa and Mayor, 2016; Friedl and Gilmour, 2009) it becomes clear that collective epithelial migration is a widespread mode that facilitates diverse morphogenesis events. Interestingly, in contrast to other collective migration phenomena, such as border-cell migration in *Drosophila*, migration of posterior lateral line primordium in zebrafish or wound healing (Scarpa and Mayor, 2016; Friedl and Gilmour, 2009), rim cell migration lacks specific leader cells. Nevertheless, even without leader cells, rim migration occurs in a very directional manner and lamellipodia formation is highly biased towards the direction of movement. This molecular and cellular directionality could possibly emerge from the distribution of forces present in the developing optic cup and/or the spatial distribution of surrounding ECM. Future studies will need to investigate these factors to understand how they influence directionality of rim migration.

Defects in rim migration lead to ectopic fate specification and interfere with future retinal development

Our data show that collective rim migration is indispensable for shaping the RNE, the organ precursor that gives rise to the retina. Rim migration translocates prospective neuroepithelial cells that initially reside in the epithelial sheet outside the optic cup to their correct location in the hemispheric RNE, where they are crucially needed for later neurogenesis events. However, when these cells do not reach the RNE in time, they change their morphology and adhere stably to the underlying ECM at ectopic positions generating a negative feedback, as these cells can never be translocated further. Thus, timely controlled rim cell migration is critical to coordinate spatial positioning of cells with the timing of neuroepithelial fate determination. Other studies investigating the formation of the neural tube have shown that, in specific circumstances, cell fate can be uncoupled from developmental position or developmental timing (Tawk et al., 2007; Girdler et al.,

2013). However, these experiments were based mainly on heterotypic cell transplantation that induced mispositioning of cells. In contrast, we show here how cells that are *naturally* located at the 'wrong position' (i.e. the opposite side of the optic vesicle) undergo a correcting migration process to end up at the necessary position to form part of the RNE. Failure of rim movement leads to enduring defects in optic cup architecture. This is highlighted by the observation that, in severe cases, a secondary invagination zone and even a secondary lens-like structure can be formed. Our study thereby reveals that RNE fate is independent of the position of cells, suggesting that while signaling pathways and patterning molecules are very important for RNE fate specification (Fuhrmann, 2010), they cannot ensure proper positioning of cells if epithelial rearrangements depending on single cell and tissue morphogenesis are impaired.

Rim migration may be a conserved process, as these cell movements have not only been observed in zebrafish and medaka but also during chick RNE morphogenesis (Kwan et al., 2011). However, rim movement has not been reported during RNE morphogenesis of organoid cultures (Eiraku et al., 2011; Nakano et al., 2012). Here, high proliferation in the RNE layer enclosed by rigid edges leads to inward bending of the developing RNE. It will now be interesting to take a closer look and investigate whether rim involution also plays a role in these *in vitro* systems.

Material and Methods

Zebrafish strains and transgenic lines

Wild type strains (WT-AB, WT-TL) and transgenic lines Tg(actb1:GFP-utrCH), (Behrndt et al., 2012), Tg(actb1:myl12.1-EGFP) (Maitre et al., 2012), Tg(*vsx2*::GFP) (Kimura et al., 2006), Tg(βactin:mKate2-ras) were used. Zebrafish were maintained and bred at

26.5°C. Embryos were raised at 28°C and then transferred to 21°C at around 80% epiboly to slow down development. At 8 ss embryos were transferred back and maintained henceforth at 28°C. All animal work was performed in accordance with European Union (EU) directive 2011/63/EU as well as the German Animal Welfare Act.

Morpholino, RNA and Plasmid injections

For morpholino-mediated knockdown of gene function, the following amounts of morpholinos were injected in the yolk at one-cell stage:

0.4 ng *laminin α-1* MO 5' TCATCCTCATCTCCATCATCGCTCA3' (Randlett et al., 2011), 3.8 ng *ojoplano* MO 5'ggactcacccaTCAGAAATTCAGCC3' (Martinez-Morales et al., 2009), 1.6 ng *ezrin* MO 5'GATGTAGATGCCGATTCCTCTCGTC3' (Link, 2006).

For whole tissue labeling, RNA was injected at the one-cell stage. For mosaic labeling of cells, either DNA was injected at one-cell stage or RNA was injected in a single blastomere at 16- to 32-cell stage. RNA was synthesized using the Ambion mMessage mMachine kit and injected at 50-60pg per embryo, whereas DNA was injected at 15 pg per embryo.

Constructs

pCS2+mKate2-ras (Weber et al., 2014), pCS2+GFP-ras (kind gift from A. Oates), pCS2+Par3-GFP (Tawk et al., 2007), pCS2+GFP-UtrophinCH (Norden et al., 2009), pCS2+DD-MRLC-GFP (Norden et al., 2009), pCS2+ EMTB-tdTomato (kind gift from D. Gilmour), βactin::mKate2-ras (Icha et al, unpublished), pCS2+Paxillin-mKate, pCS2+ Integrinβ1b-mKate, hsp::GFP-Utrophin (Strzyz et al., 2015), hsp70::EGFP-Rac1T17N, hsp::mKate2-Rac1T17N (for cloning strategies see supplemental Material and Methods).

Heat-shock-driven gene expression

Embryos injected with heat-shock-driven constructs were incubated at 15 ss at 37°C for 20 min.

Drug treatments

Dechorionated embryos were incubated in the drug solutions made in E3 medium. Rockout and Aphidicolin were dissolved in DMSO. Hydroxyurea was dissolved in water. Rockout was used at 100 µM with 0.1% DMSO (by volume) in E3. During live imaging, Rockout was used at 125 µM. For inhibition of cell proliferation, embryos were treated with a mixture of 30 mM HU and 210 µM Aphidicolin. Equivalent amounts of DMSO were added as solvent control.

Immunostaining

Embryos were fixed with 4% PFA in PBS overnight at 4°C, followed by permeabilisation using PBT (PBS with 0.8% Triton X-100). To improve permeability, embryos were trypsinized on ice for 15 min, followed by blocking with 10% normal goat serum and incubated in the primary antibody mix with 1% NGS in PBT for 60 h at 4°C. After washing, embryos were incubated with secondary antibody mix with 1% NGS in PBT for 60 h. The embryos were mounted either in agarose or in 80% glycerol.

The following dilutions were used. Primary antibodies: 1:50 anti-phospho-myosin (Cell signaling 3671), 1:100 anti-laminin (Sigma L-9393), 1:100 anti-chondroitin sulphate CS-56 (Abcam ab11570), 1:100 anti-fibronectin (Sigma F3648), 1:500 anti-pH3 (Abcam ab10543), 1:500 anti-tRFP (Evrogen AB233), 1:100 anti-GFP (Milipore MAB3580).

Secondary antibodies and fluorescent markers: Alexa Fluor 488 anti-Rabbit (Invitrogen A21206), Rhodamine-Phalloidin (1:50), DAPI.

Image Acquisition

Brightfield imaging

Embryos were anaesthetized with 0.04% MS-222 (Sigma) and mounted on a drop of 3% methylcellulose in E3 medium. Images were taken on a Leica M165C scope with an MC170 HD camera.

In Vivo Time-Lapse Imaging

Embryos were mounted in 0.6% low melt agarose in E3 medium on Mattek glass bottom dishes for spinning disk confocal microscopy and in a capillary for Lightsheet microscopy. Embryos were anaesthetized using 0.04% MS-222 (Sigma).

An Andor spinning disk system with a 40x silicon oil objective (NA=1.25) was used with a heating chamber; z stacks of 90 µm were acquired with optical section of 0.7 µm every 3-5min for about 6-7 h. For live imaging of GFP-UtrophinCH, myl12.1-EGFP transgenic embryos and paxillin-mKate injected embryos (All Figure 1 and Figure S2), a Zeiss Lightsheet Z.1 microscope with a Zeiss Plan-Apochromat 20x water-dipping objective (NA=1.0) and sample chamber heated to 28°C was used.

Confocal Scans

Imaging was performed on Zeiss LSM 710 confocal microscopes with a 40x water-immersion objective (NA=1.2).

Image analysis

RNE cell apical and basal footprint analysis

Footprints of the RNE cells were measured by analyzing the optical section below the developing lens placode for basal footprints and apical side of the same cells for apical footprints. A rectangular area was marked where the apical and basal endfeet were

observable. The number of cells in this area was calculated using multipoint tool in Fiji (Schindelin et al., 2012). Cells, which were partially overlapping in the field, were counted only on left and top border of the rectangle.

Actomyosin distribution analysis

The average distribution of actomyosin along the apicobasal axis of the RNE was measured using a custom-made Fiji macro (Benoit Lombardot). The region of interest (ROI) was defined as a 10 µm x 10 µm x h cuboid, with h corresponding to the height of the apicobasal axis of the RNE layer. Using this ROI, an average intensity value was calculated for each point along the apicobasal axis normalized to 100. To compare across samples, the average intensities were normalized to the highest average intensity value along the axis. This was calculated for 5 different regions each in multiple optic cups.

Invagination angle analysis

The invagination angle was measured manually as the angle held at the center of the cup by the inner lips of the optic cup using the angle tool in Fiji. The angle was measured at three different central optical sections in an optic cup and the average value was used as the angle of invagination.

Rim cell speed analysis

The basal side of the migrating cells was tracked using MTrackJ plugin in Fiji (Meijering et al., 2012). The cell speed was calculated as a ratio of the track length to the track duration.

Statistical analysis and graphical representation was performed using the Prism software package.

Author contributions

Conceptualization C.N., J.S.; Methodology, J.S., C.N.; Investigation, J.S., N.I.; Writing – Original Draft, C.N., J.S.; Writing – Review & Editing, C.N., J.S.; Visualization, J.S.; Supervision C.N., J.S.

Acknowledgements

We thank Y. Bellaiche, E. Knust, J. Martinez-Morales, D. Mateju, M. Palfy, and I.K. Patten for helpful comments on the manuscript. We also thank the Norden lab for useful discussions, B. Lombardot for the plugin allowing analysis of actomyosin distribution. C. Fröb, J. Icha, M. Palfy, S. Schneider, I. Yanakieva are thanked for experimental help. The light microscopy and fish facility are also thanked. D. Gilmour, C. Henry and A. Oates for sharing constructs.

J.S. is a member of the IMPRS-CellDevoSys PhD program and supported by a fellowship by the DIGS-BB. C.N. was supported by the Human Frontier Science Program (CDA-00007/2011) and the German Research Foundation (DFG). The authors declare no conflict of interest.

References

Bazin-Lopez, N., L.E. Valdivia, S.W. Wilson, and G. Gestri. 2015. Watching eyes take shape. *Current Opinion in Genetics & Development*. 32:73–79. doi:10.1016/j.gde.2015.02.004.

Behrndt, M., G. Salbreux, P. Campinho, R. Hauschild, F. Oswald, J. Roensch, S.W. Grill, and C.-P. Heisenberg. 2012. Forces driving epithelial spreading in zebrafish gastrulation. *Science*. 338:257–260. doi:10.1126/science.1224143.

Bogdanović, O., M. Delfino-Machín, M. Nicolás-Pérez, M.P. Gavilán, I. Gago-Rodrigues, A. Fernández-Miñán, C. Lillo, R.M. Ríos, J. Wittbrodt, and J.R. Martínez-Morales. 2012. Numb/Numbl-Opo Antagonism Controls Retinal Epithelium Morphogenesis by Regulating Integrin Endocytosis. *Dev.Cell.* 23:782–795. doi:10.1016/j.devcel.2012.09.004.

Bryan, C.D., C.-B. Chien, and K.M. Kwan. 2016. Loss of laminin alpha 1 results in

multiple structural defects and divergent effects on adhesion during vertebrate optic cup morphogenesis. *Dev Biol*. 1–14. doi:10.1016/j.ydbio.2016.06.025.

Dominguez-Gimenez, P., N.H. Brown, and M.D. Martin-Bermudo. 2007. Integrin-ECM interactions regulate the changes in cell shape driving the morphogenesis of the Drosophila wing epithelium. *J Cell Sci*. 120:1061–1071. doi:10.1242/jcs.03404.

Durdu, S., M. Iskar, C. Revenu, N. Schieber, A. Kunze, P. Bork, Y. Schwab, and D. Gilmour. 2014. Luminal signalling links cell communication to tissue architecture during organogenesis. *Nature*. 515:120–124. doi:10.1038/nature13852.

Eiraku, M., N. Takata, H. Ishibashi, M. Kawada, E. Sakakura, S. Okuda, K. Sekiguchi, T. Adachi, and Y. Sasai. 2011. Self-organizing optic-cup morphogenesis in three-dimensional culture. *Nature*. 472:51–56. doi:doi:10.1038/nature09941.

Friedl, P., and D. Gilmour. 2009. Collective cell migration in morphogenesis, regeneration and cancer. *Nat Rev Mol Cell Biol*. 10:445–457. doi:10.1038/nrm2720.

Friedl, P., and K. Wolf. 2010. Plasticity of cell migration: a multiscale tuning model. *J. Cell Biol*. 188:11–19. doi:10.1083/jcb.200909003.

Fuhrmann, S. 2010. Chapter Three - Eye Morphogenesis and Patterning of the Optic Vesicle. 93. Elsevier Inc. 24 pp.

Gago-Rodrigues, Fernández-Miñán A, Letelier J, Naranjo S, Tena JJ, Gómez-Skarmeta JL, Martinez-Morales JR. (. 2015. Analysis of opo cis-regulatory landscape uncovers Vsx2 requirement in early eye morphogenesis. *Nat Comms*. 6:1–13. doi:10.1038/ncomms8054.

Girdler, G.C., C. Araya, X. Ren, and J.D.W. Clarke. 2013. Developmental time rather than local environment regulates the schedule of epithelial polarization in the zebrafish neural rod. *Neural Dev*. 8:5. doi:10.1186/1749-8104-8-5.

Greene, N.D.E., and A.J. Copp. 2014. Neural Tube Defects. *Annu. Rev. Neurosci.* 37:221–242. doi:10.1146/annurev-neuro-062012-170354.

Guillot, C., and T. Lecuit. 2013. Mechanics of epithelial tissue homeostasis and morphogenesis. *Science*. 340:1185–1189. doi:10.1126/science.1235249.

Gutzman, J.H., E.G. Graeden, L.A. Lowery, H.S. Holley, and H. Sive. 2008. Formation of the zebrafish midbrain–hindbrain boundary constriction requires laminin-dependent basal constriction. *Mech Dev*. 125:974–983. doi:10.1016/j.mod.2008.07.004.

Haigo, S.L., and D. Bilder. 2011. Global tissue revolutions in a morphogenetic movement controlling elongation. *Science*. 331:1071–1074. doi:10.1126/science.1199424.

Harris, W.A., and V. Hartenstein. 1991. Neuronal determination without cell division in Xenopus embryos. *Neuron* 6:499–515.

Heermann, S., L. Schütz, S. Lemke, K. Krieglstein, and J. Wittbrodt. 2015. Eye morphogenesis driven by epithelial flow into the optic cup facilitated by modulation of

bone morphogenetic protein. *Elife*. 4:373. doi:10.7554/eLife.05216.

Ivanovitch, K., F. Cavodeassi, and S.W. Wilson. 2013. Precocious acquisition of neuroepithelial character in the eye field underlies the onset of eye morphogenesis. *Dev.Cell.* 27:293–305. doi:10.1016/j.devcel.2013.09.023.

Kimura, Y., Y. Okamura, and S.-I. Higashijima. 2006. alx, a zebrafish homolog of Chx10, marks ipsilateral descending excitatory interneurons that participate in the regulation of spinal locomotor circuits. *Journal of Neuroscience*. 26:5684–5697. doi:10.1523/JNEUROSCI.4993-05.2006.

Kwan, K.M., H. Otsuna, H. Kidokoro, K.R. Carney, Y. Saijoh, and C.B. Chien. 2011. A complex choreography of cell movements shapes the vertebrate eye. *Development*. 139:359–372. doi:10.1242/dev.071407.

Lecuit, T., and L. Le Goff. 2007. Orchestrating size and shape during morphogenesis. *Nature*. 450:189–192. doi:10.1038/nature06304.

Leptin, M. 2005. Gastrulation movements: the logic and the nuts and bolts. *DEVCEL*. 8:305–320. doi:10.1016/j.devcel.2005.02.007.

Link V, Carvalho L, Castanon I, Stockinger P, Shevchenko A, Heisenberg CP.(2006). *J Cell Sci*. 119:2073–2083. doi:10.1242/jcs.02928.

Lodyga, M., X.-H. Bai, A. Kapus, and M. Liu. 2010. Adaptor protein XB130 is a Rac-controlled component of lamellipodia that regulates cell motility and invasion. *J Cell Sci*. 123:4156–4169. doi:10.1242/jcs.071050.

Maitre, J.L., H. Berthoumieux, S.F.G. Krens, G. Salbreux, F. Julicher, E. Paluch, and C.-P. Heisenberg. 2012. Adhesion Functions in Cell Sorting by Mechanically Coupling the Cortices of Adhering Cells. *Science*. 338:253–256. doi:10.1126/science.1225399.

Martinez-Morales, J.R., M. Rembold, K. Greger, J.C. Simpson, K.E. Brown, R. Quiring, R. Pepperkok, M.D. Martin-Bermudo, H. Himmelbauer, and J. Wittbrodt. 2009. ojoplano-mediated basal constriction is essential for optic cup morphogenesis. *Development*. 136:2165–2175. doi:10.1242/dev.033563.

Meijering, E., O. Dzyubachyk, and I. Smal. 2012. Methods for cell and particle tracking. *Meth. Enzymol.* 504:183–200. doi:10.1016/B978-0-12-391857-4.00009-4.

Morata, G. 2001. How Drosophila appendages develop. *Nat Rev Mol Cell Biol*. 2:89–97. doi:10.1038/35052047.

Nakano, T., S. Ando, N. Takata, M. Kawada, K. Muguruma, K. Sekiguchi, K. Saito, S. Yonemura, M. Eiraku, and Y. Sasai. 2012. Self-Formation of Optic Cups and Storable Stratified Neural Retina from Human ESCs. *STEM*. 10:771–785. doi:10.1016/j.stem.2012.05.009.

Norden, C., S. Young, B.A. Link, and W.A. Harris. 2009. Actomyosin is the main driver of interkinetic nuclear migration in the retina. *Cell*. 138:1195–1208.

doi:10.1016/j.cell.2009.06.032.

Picker, A., F. Cavodeassi, A. Machate, S. Bernauer, S. Hans, G. Abe, K. Kawakami, S.W. Wilson, and M. Brand. 2009. Dynamic Coupling of Pattern Formation and Morphogenesis in the Developing Vertebrate Retina. *PLoS Biol*. 7:e1000214. doi:10.1371/journal.pbio.1000214.s014.

Randlett, O., L. Poggi, F.R. Zolessi, and W.A. Harris. 2011b. The Oriented Emergence of Axons from Retinal Ganglion Cells Is Directed by Laminin Contact in Vivo. *Neuron.* 70:266–280. doi:10.1016/j.neuron.2011.03.013.

Scarpa, E., and R. Mayor. 2016. Collective cell migration in development. *J Cell Biol*. 212:143–155. doi:10.1083/jcb.201508047.

Schepis, A., D. Sepich, and W.J. Nelson. 2012. E-catenin regulates cell-cell adhesion and membrane blebbing during zebrafish epiboly. *Development*. 139:537–546. doi:10.1242/dev.073932.

Schindelin, J., I. Arganda-Carreras, E. Frise, V. Kaynig, M. Longair, T. Pietzsch, S. Preibisch, C. Rueden, S. Saalfeld, B. Schmid, J.-Y. Tinevez, D.J. White, V. Hartenstein, K. Eliceiri, P. Tomancak, and A. Cardona. 2012. Fiji: an open-source platform for biological-image analysis. *Nat Meth*. 9:676–682. doi:10.1038/nmeth.2019.

Strzyz, P.J., H.O. Lee, J. Sidhaye, I.P. Weber, L.C. Leung, and C. Norden. 2015. Interkinetic Nuclear Migration Is Centrosome Independent and Ensures Apical Cell Division to Maintain Tissue Integrity. *Dev.Cell.* 32:203–219. doi:10.1016/j.devcel.2014.12.001.

Subauste, M.C., M. Von Herrath, V. Benard, C.E. Chamberlain, T.H. Chuang, K. Chu, G.M. Bokoch, and K.M. Hahn. 2000. Rho family proteins modulate rapid apoptosis induced by cytotoxic T lymphocytes and Fas. *J Biol Chem*. 275:9725–9733.

Tawk, M., C. Araya, D.A. Lyons, A.M. Reugels, G.C. Girdler, P.R. Bayley, D.R. Hyde, M. Tada, and J.D.W. Clarke. 2007. A mirror-symmetric cell division that orchestrates neuroepithelial morphogenesis. *Nature*. 446:797–800. doi:10.1038/nature05722.

Weber, I.P., A.P. Ramos, P.J. Strzyz, L.C. Leung, S. Young, and C. Norden. 2014. Mitotic position and morphology of committed precursor cells in the zebrafish retina adapt to architectural changes upon tissue maturation. *CellReports*. 7:386–397. doi:10.1016/j.celrep.2014.03.014.

Yarrow, J.C., G. Totsukawa, G.T. Charras, and T.J. Mitchison. 2005. Screening for Cell Migration Inhibitors via Automated Microscopy Reveals a Rho-Kinase Inhibitor. *Chemistry & Biology*. 12:385–395. doi:10.1016/j.chembiol.2005.01.015

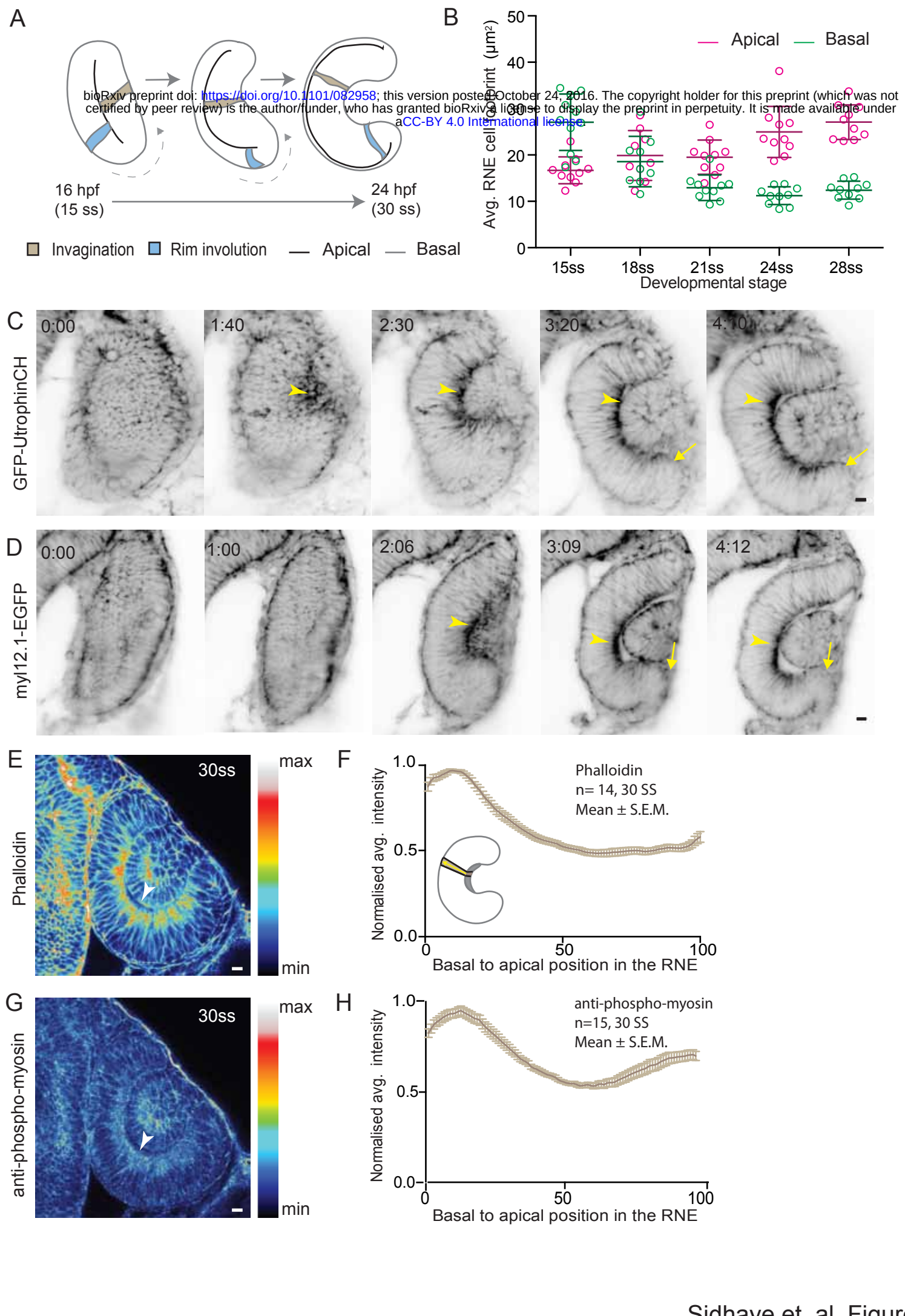

Sidhaye et. al. Figure 1

Figure 1: RNE invagination is accompanied by basal foot shrinkage and basal actomyosin accumulation.

A) Schematic representation of RNE morphogenesis from 16 hours post fertilization (hpf) or 15 somite stage (ss) to 24 hpf or 30 ss with central RNE cells (brown) that undergo invagination and rim cells (blue) that undergo rim involution. Dotted arrow marks direction of rim involution.

B) Average footprint of RNE cells at apical (magenta) and basal (green) sides during RNE morphogenesis with mean ± SD. N=10 embryos.

C, D) Time-lapse imaging of RNE morphogenesis to asses dynamics of actin marked by GFP-UtrophinCH (C) and of myosin marked by myl12.1-EGFP (D). Arrowhead marks basal enrichment in RNE. Arrow marks the rim zone lacking basal enrichment. Movies started around 15 ss. Time in h:min.

E, G) Confocal scan of optic cup at 30 ss immunostained for phalloidin (E) and phosphomyosin (G). The arrowhead marks enrichment at the basal side of the RNE. Lookup table indicates maximum and minimum intensity values.

F, H) Normalized average intensity distributions of phalloidin (F) and phosphomyosin (H) in the tissue volume along the apicobasal axis of the RNE at 30 ss. Mean±SEM. The schematic shows a typical tissue section used for analysis. Tissue sections, n=14 for phalloidin and n=15 for phosphomyosin; N=5 embryos. All scale bars=10 μm. See also Figure S1.

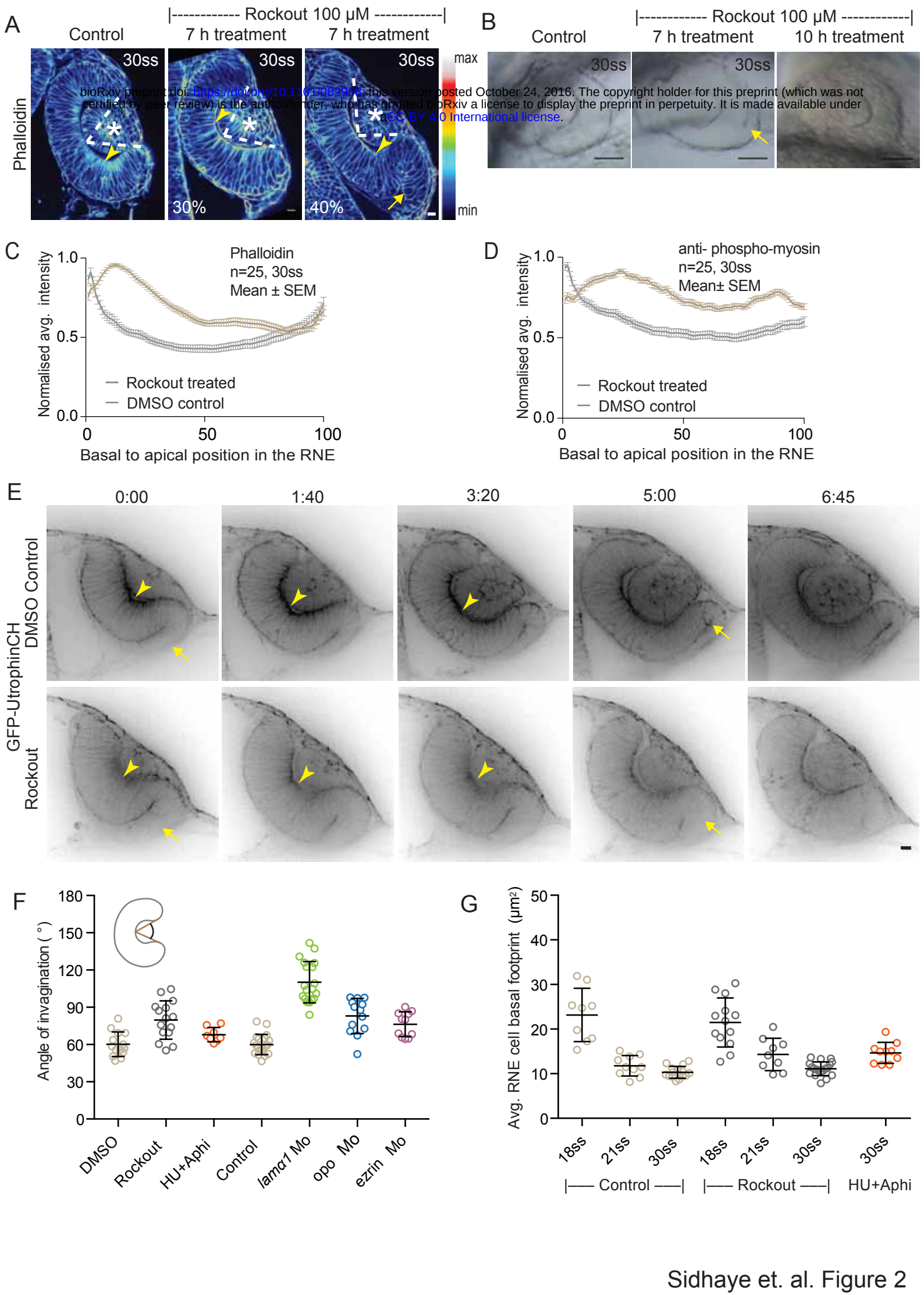

Sidhaye et. al. Figure 2

Figure 2: Impairment of actomyosin-driven basal constriction or proliferation does not prevent RNE formation

A) Confocal scan of optic cup at 30 ss stained for phalloidin. Control (left), phenotypes after 7 h of Rockout treatment: invagination defect in 30% embryos (middle), invagination defect with epithelial accumulation in 40% embryos (right), (n=30 embryos, N=4 experiments). Arrowheads mark the basal side of the RNE. Arrow marks the epithelial accumulation outside the RNE. Asterisk marks the developing lens. Dashed lines indicate angle of invagination. Scale bar=10 μm.

B) Brightfield images of 30 ss RNE. Control (left), Treated with Rockout for 7 h (middle) and for 10 h (right). Arrow marks the epithelial accumulation outside the RNE. Scale bar=50 μm.

C,D) Normalized average intensity distributions of phalloidin (C) and phosphomyosin (D) in the tissue volume along the apicobasal axis of the RNE at 30 ss. Mean ± SEM. Control (brown), Rockout treated (green). Tissue sections, n=25; N=5 embryos.

E) Time-lapse of RNE morphogenesis in DMSO Control (upper) and Rockout-treated (lower) embryos expressing actin marker GFP-UtrophinCH. Rockout treatment was started 2 h before imaging. Imaging started at around 18ss. Time in h:min. Both movies were imaged simultaneously and under identical imaging conditions. Scale bar=10 μm.

F) Invagination angle at 30 ss. Mean±SD The schematic shows the invagination angle as the angle held at the base of central RNE by the inner lips of the optic cup. P values for Mann-Whiney test are as follows: Rock-out p=0.0004, HU+Aphi p=0.0421 and for laminin a1 Mo, opo Mo and ezrin Mo p<0.0001.

G) Average basal footprint of RNE cells with mean ± SD. Each dot represents an embryo. See also Figure S2.

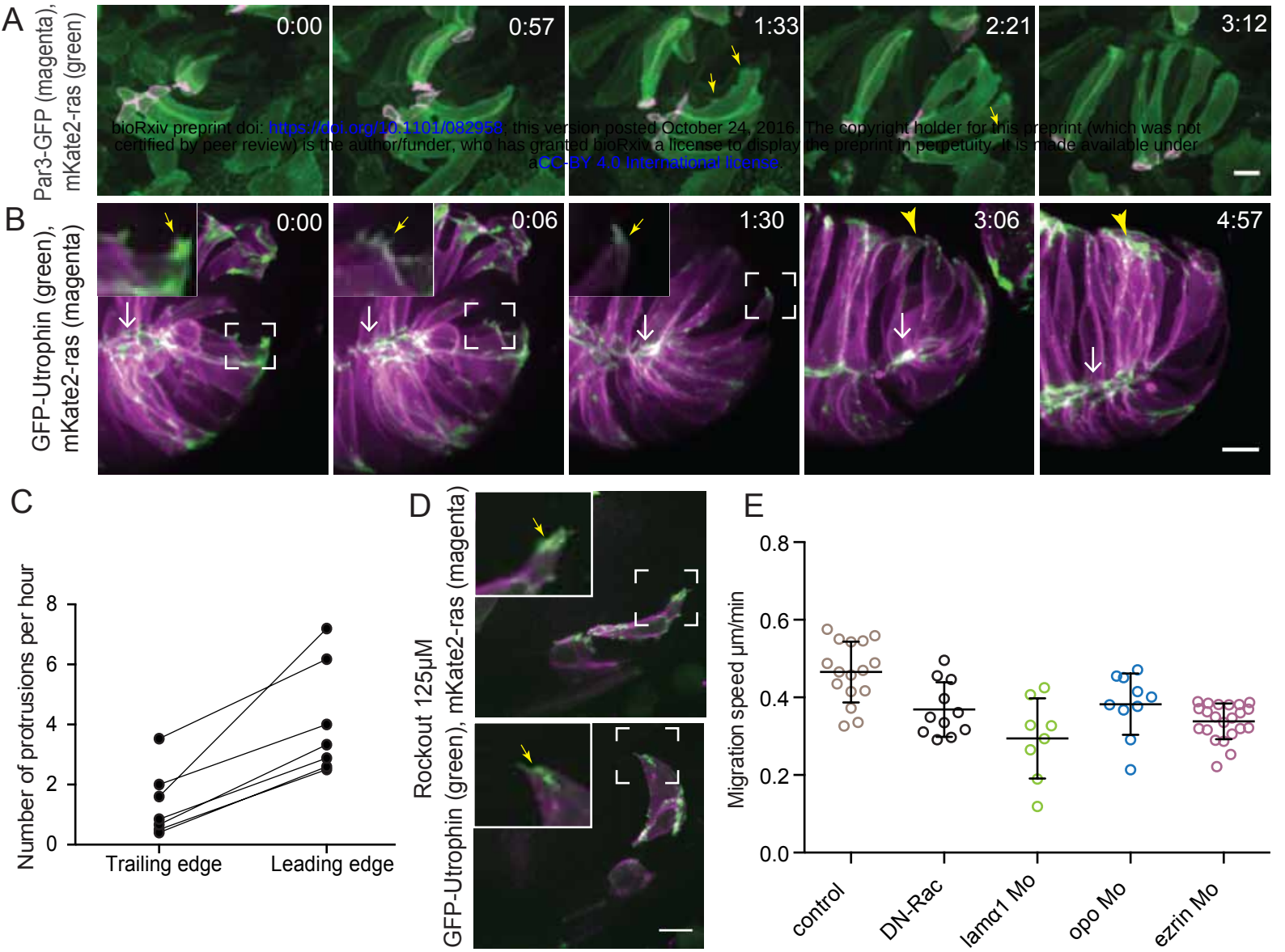

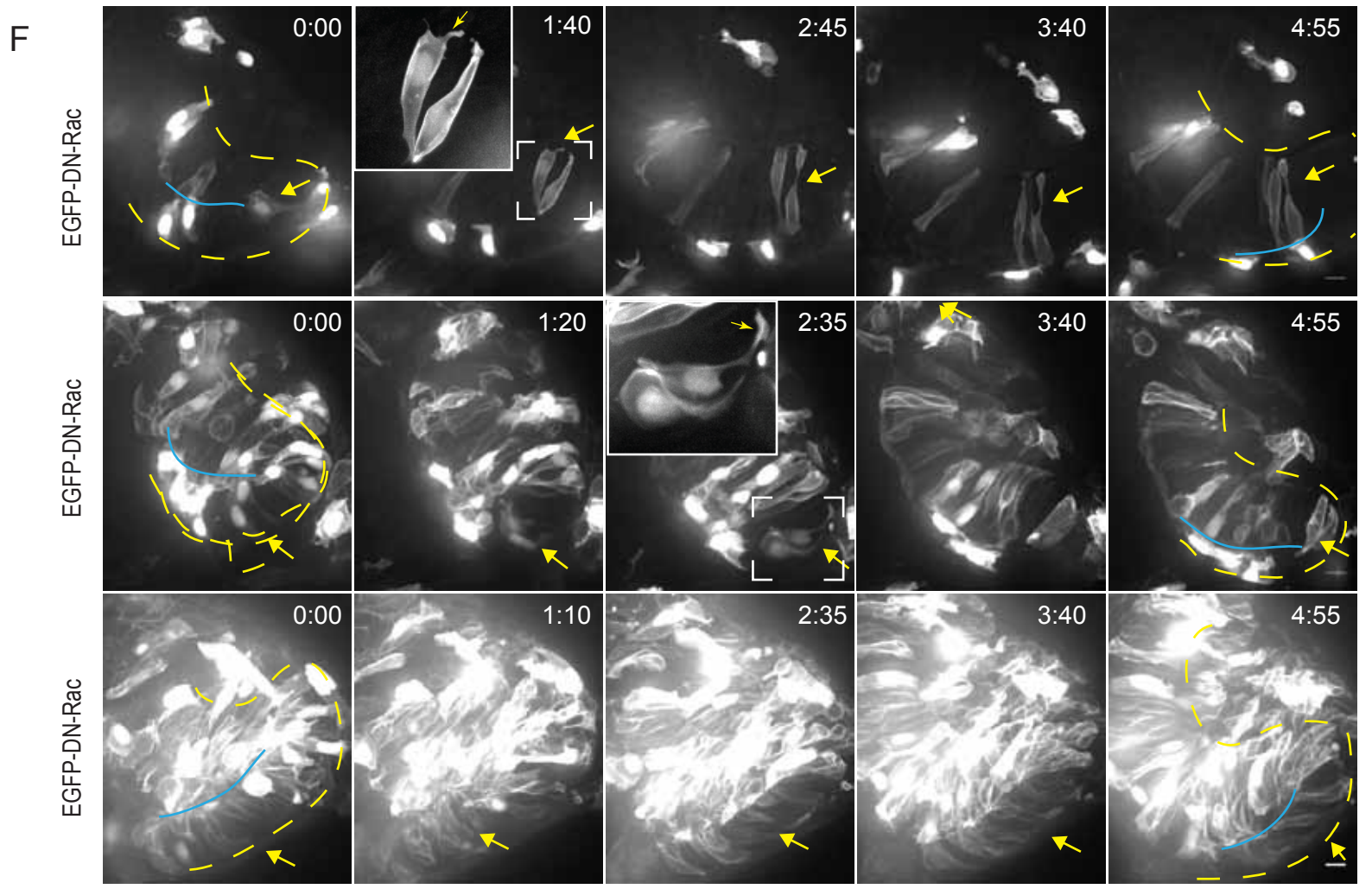

Sidhaye et. al. Figure 3

Figure 3: Rim involution involves active collective cell migration

A) Time-lapse imaging of rim zone with mosaic expression of Par3-GFP and mKate2-ras. Inlays show enlarged marked area. Yellow arrows show membrane protrusions.
B) Time-lapse imaging of rim zone with mosaic expression of GFP-UtrophinCH and ras-mKate2. Inlays show zoomed marked area. Yellow arrows show actin localization in the protrusions. White arrows mark adherens junctions. Arrowheads mark basally enriched stable actin pool in the RNE.
C) Number of protrusions observed per hour in the rim cell. Each pair of datapoints represents two sides of the same rim cell. n=7 cells
D) Confocal scan of rim zone in Rockout-treated embryos with mosaic expression of GFP-UtrophinCH and ras-mKate2. Inlays show enlarged marked area. Yellow arrows
show actin localization in the protrusions.
E) Migration speed of rim cells (Mean±SD). P values for Mann Whitney test: DN-Rac P=0.0039 laminin Mo P=0.0004, opo Mo P=0.0176, ezrin Mo P <0.0001.
F) Time-lapse imaging of RNE morphogenesis with mosaic expression of hsp70::EFGP-DN-Rac. The degree of mosaic expression varies from highly mosaic (Upper), moderately mosaic (middle) to less mosaic (lower). Inlays show the abnormal morphology of DN-Rac expressing cell. Yellow dashed line marks the outline of the developing RNE. Blue line marks the apical side in the rim zone. Heat-shock at 12 ss. Imaging started 3 hours after heat shock. Note that the delay in rim involution and RNE morphogenesis correlates with the clone size. All scale bars=10 μm. All movies started around 17 ss -18 ss, Time in h:min See also Figure S3.

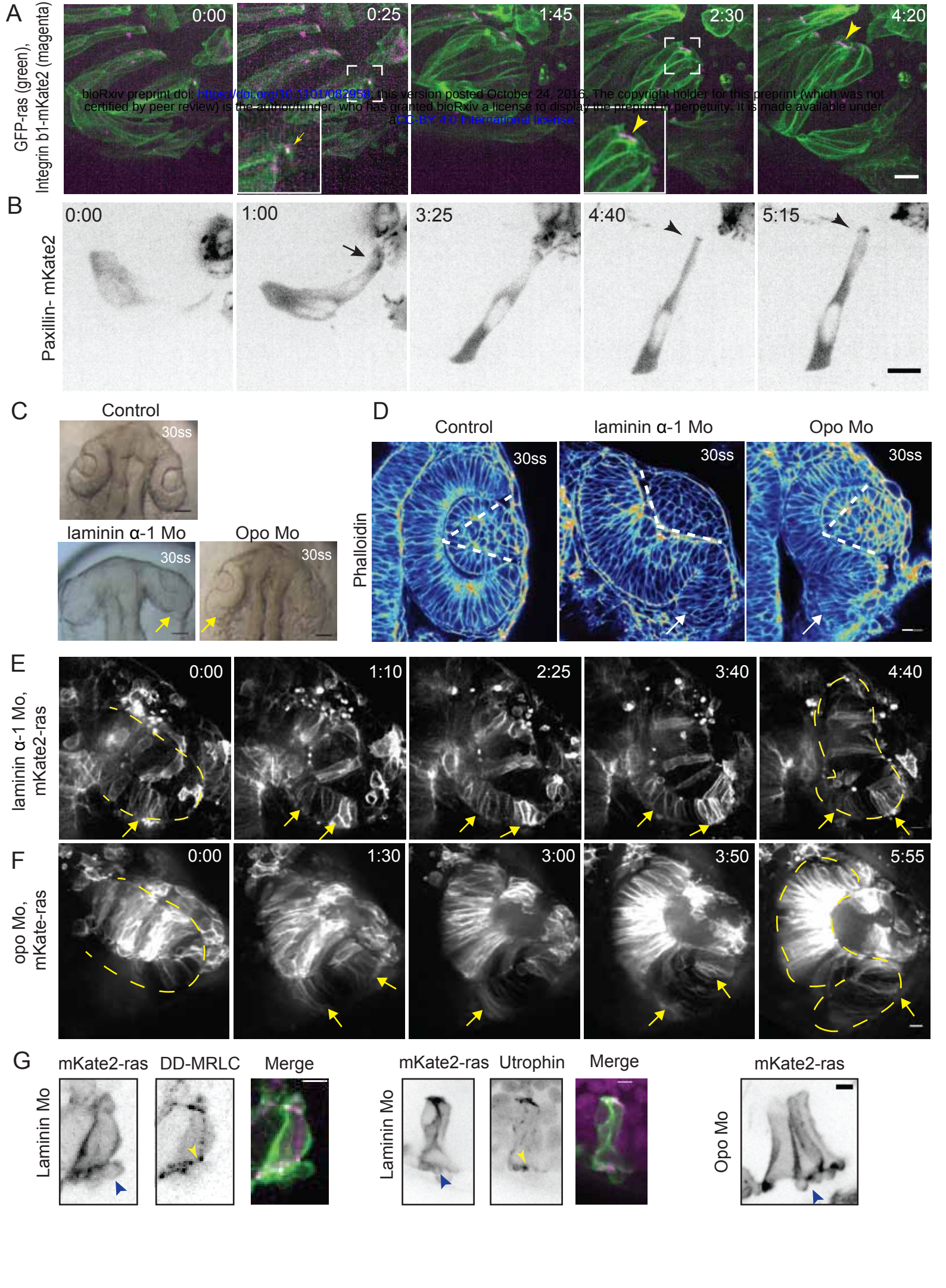

Sidhaye et. al. Figure 4

Figure 4: Dynamic cell-ECM attachments of rim cells are important for RNE morphogenesis

A) Time-lapse imaging of rim zone with mosaic expression of GFP-ras and Integrin-β1b-mKate2. Inlays show enlarged marked area. Arrow indicates the integrin foci during migration. Arrowheads mark the basally enriched stable integrin pool in the RNE cell. Scale bar=10 µm. Imaging started at 17-18 ss, Time in h:min

B) Timelapse imaging of rim zone with mosaic expression of paxillin-mKate2. Arrow indicates the short-lived paxillin punctae. Arrowhead marks the stable basal paxillin localization in the RNE. Scale bar=10 µm. Imaging started at 17-18ss. Time in h:min

C) Brightfield images of dorsal view of 30 ss embryo head. Control (upper), laminin morphant (lower left) and opo morphant (lower right). Arrows mark the epithelial accumulation outside the RNE. Scale bar=50µm

D) Confocal scan of optic cup at 30 ss stained for phalloidin. Control (left), laminin morphant (middle) and opo morphant (right). Arrows mark the epithelial accumulation outside the RNE. Dashed lines indicate the angle of invagination. Scale bar=10µm

E,F) Time-lapse imaging of RNE morphogenesis in laminin morphant (D) and Opo morphant (E) injected mosaically with mKate2-ras RNA. Arrows mark rim cells that failed to move. Dashed line marks the outline of the developing RNE. Time in h:min. Scale bar=10µm. Movies started at 16 ss -17 ss.

G) Confocal scan of rim cells exhibiting bleb-like protrusion (blue arrowhead) in laminin morphants mosaically labeled by mKate2-ras with DD-MRLC-GFP (left) and GFP-UtrophinCH (middle) and opo morphants labeled by mKate2-ras. Yellow arrowhead marks the localization of DD-MRLC outside and UtrophinCH inside the bleb. Scale bar=2 µm. See also Figure S4 and S5.

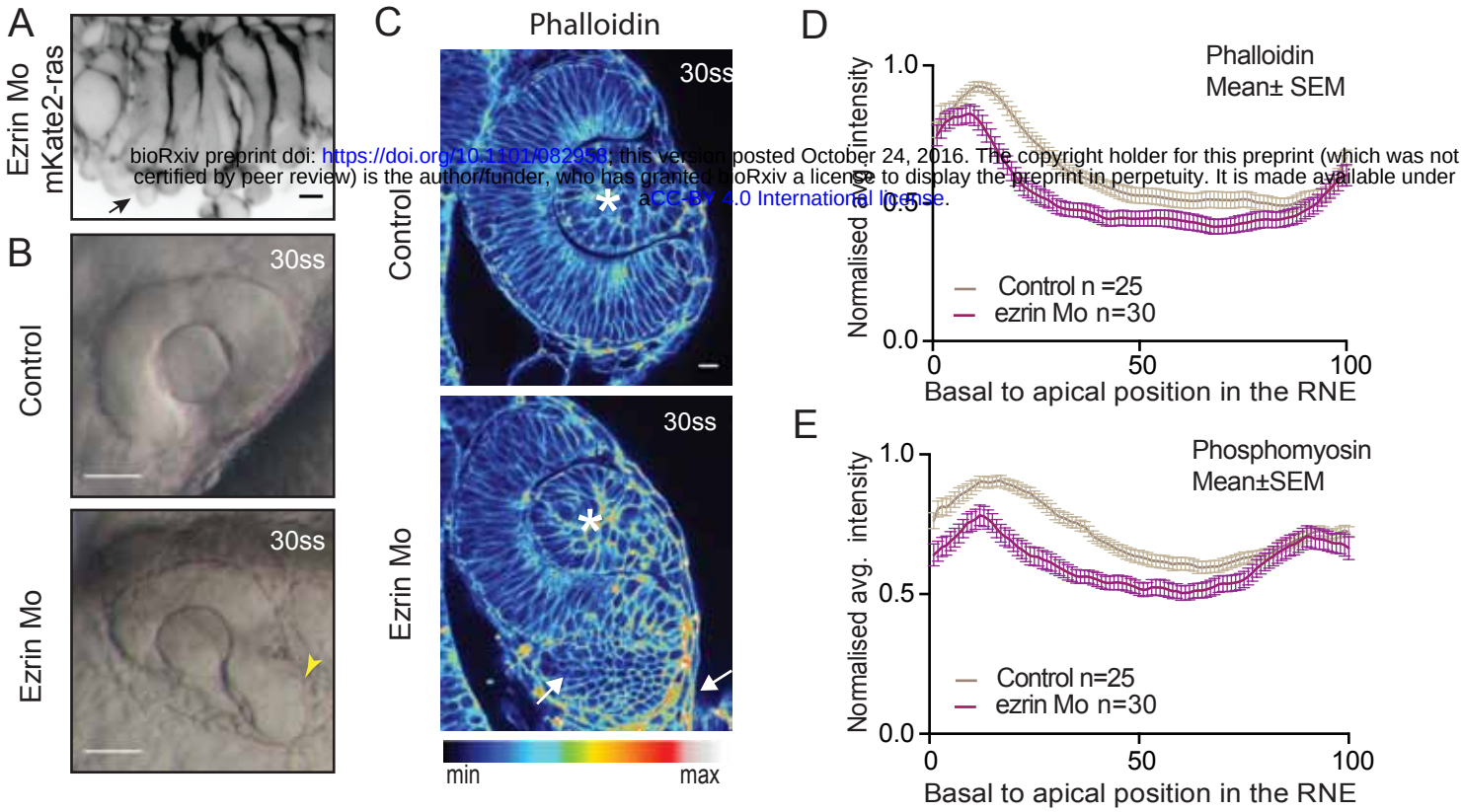

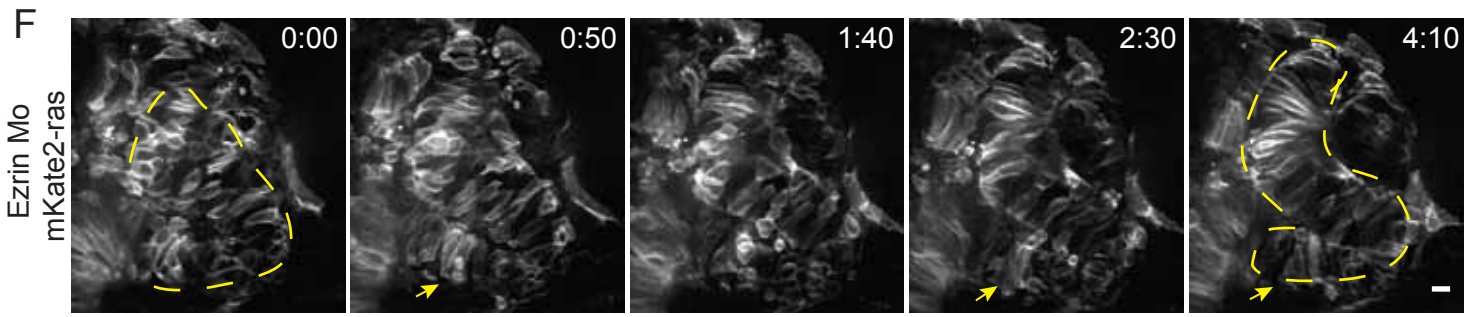

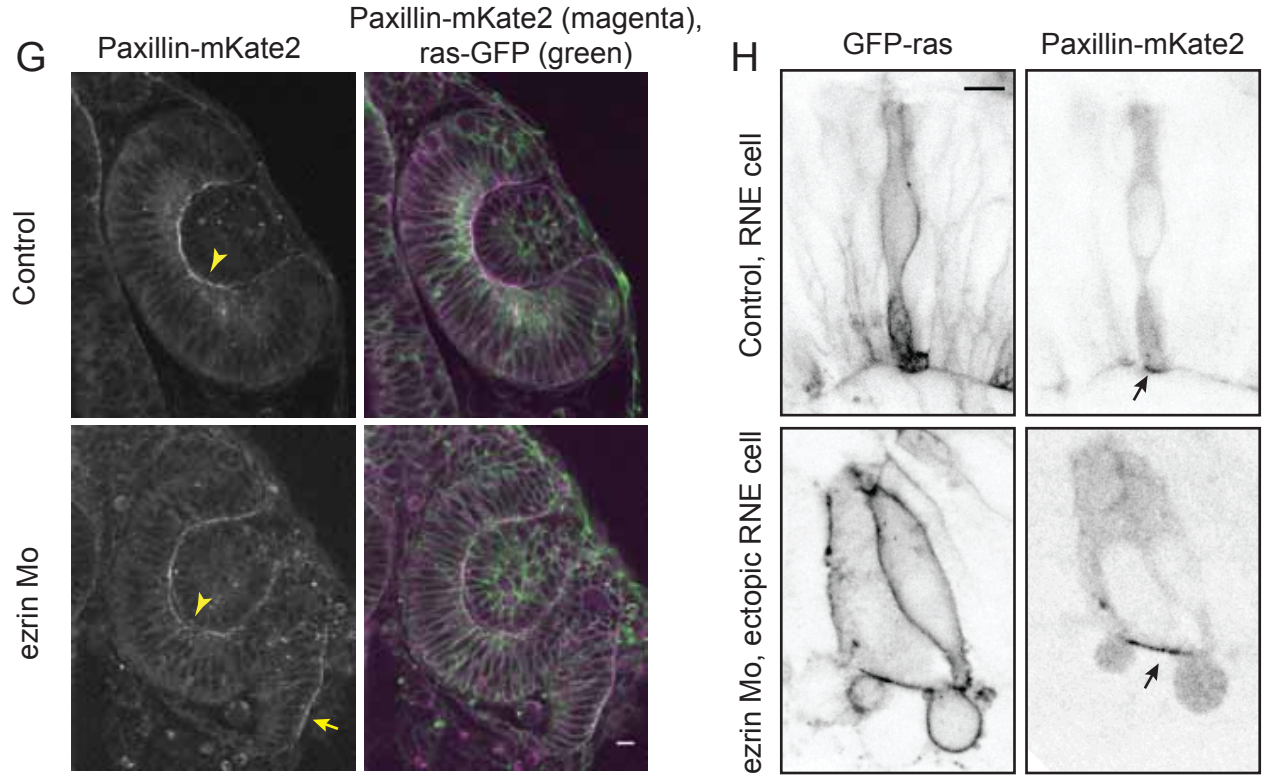

Sidhaye et. al. Figure 5

Figure 5: Forced bleb induction leads to compromised rim involution and impairs RNE morphogenesis.

A) Confocal scan of mKate2-ras injected ezrin morphants. Arrow indicates basal blebs in rim cells. Scale bar=5 µm.

B) Brightfield images of side view of 30 ss optic cup. Control (top) and ezrin morphant (bottom). Arrowhead marks the epithelial accumulation outside the RNE. Scale bar=50 µm

C) Confocal scan of optic cup at 30 ss stained for phalloidin. Control (top) and ezrin morphants (bottom). Arrows mark the epithelial accumulation outside the RNE. Asterisk marks the lens. Scale bar=10 µm

D,E) Normalized average intensity distributions of phalloidin (D) and phosphomyosin (E) in the tissue volume along the apicobasal axis of the RNE at 30 ss. Mean±SEM. Control (brown) ezrin Mo (magenta). Tissue sections, n=25 for control and n=30 for ezrin Mo; N=5 embryos.

F) Time-lapse imaging of RNE morphogenesis in ezrin morphant injected mosaically with ras-mKate2 RNA. Arrows mark rim cells that failed to move. Dashed line marks the outline of developing RNE. Time in h:min. Scale bar=10µm. Imaging started at 17 ss – 18 ss.

G) Confocal scan of 30 ss optic cup expressing paxillin-mKate2 and GFP-ras. Control (top), ezrin Mo (bottom). Arrow marks paxillin enrichment at the basal side. Scale bar=10 µm.

H) Confocal scan of paxillin-mKate2 and GFP-ras expressing cells. Control RNE cells (top), ectopic RNE cell in ezrin morphant (bottom). Arrow marks basal paxillin enrichment. Scale bar=5µm. See also Figure S5.

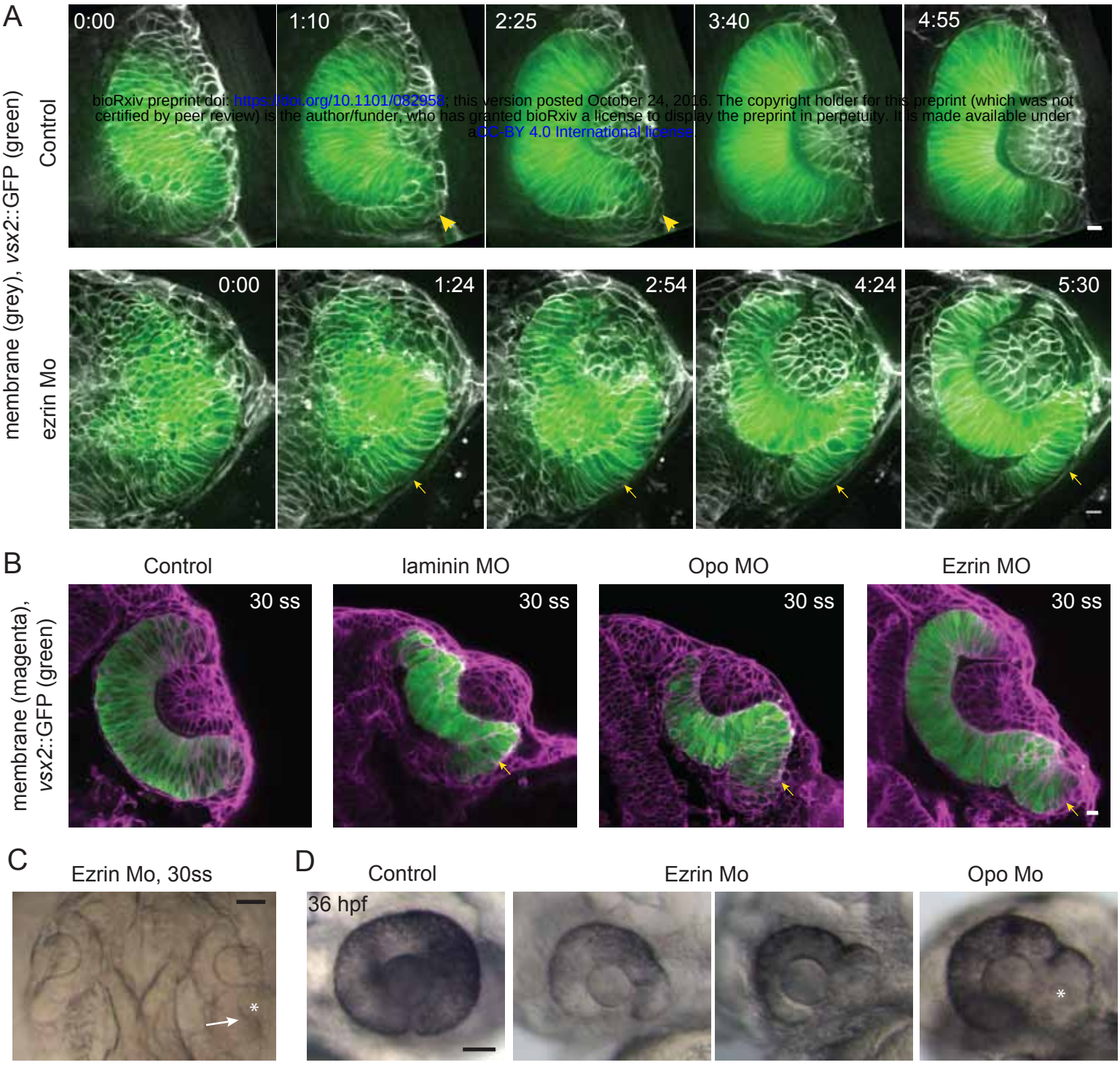

Figure 6: Impairment of rim involution leads to mispositioning of neuroepithelial cells.

A) Time-lapse imaging of control and ezrin morphant condition in Tg(vsx2::GFP, βactin::mKate2ras) background. Arrowheads mark rim zone in control. Arrows mark rim cells that failed to migrate in ezrin morphant. Time in h:min. Movies started at 16 ss -17 ss.
B) Confocal scans of optic cups at 30 ss in control, laminin morphant, Opo morphant and ezrin morphant conditions in Tg(vsx2::GFP, βactin::mKate2-ras). Embryos were stained for GFP and mKate-2
C) Brightfield image of 30 ss ezrin morphant showing secondary optic cup phenotype. Arrow marks secondary invagination zone. Asterisk marks lens-like structure.
D) Brightfield images of 36 hpf control embryos, ezrin morphants and opo morphant. Asterisk marks extra lens-like structure.
Scale bars in (A,B)=10 µm and (C,D)=50 µm.

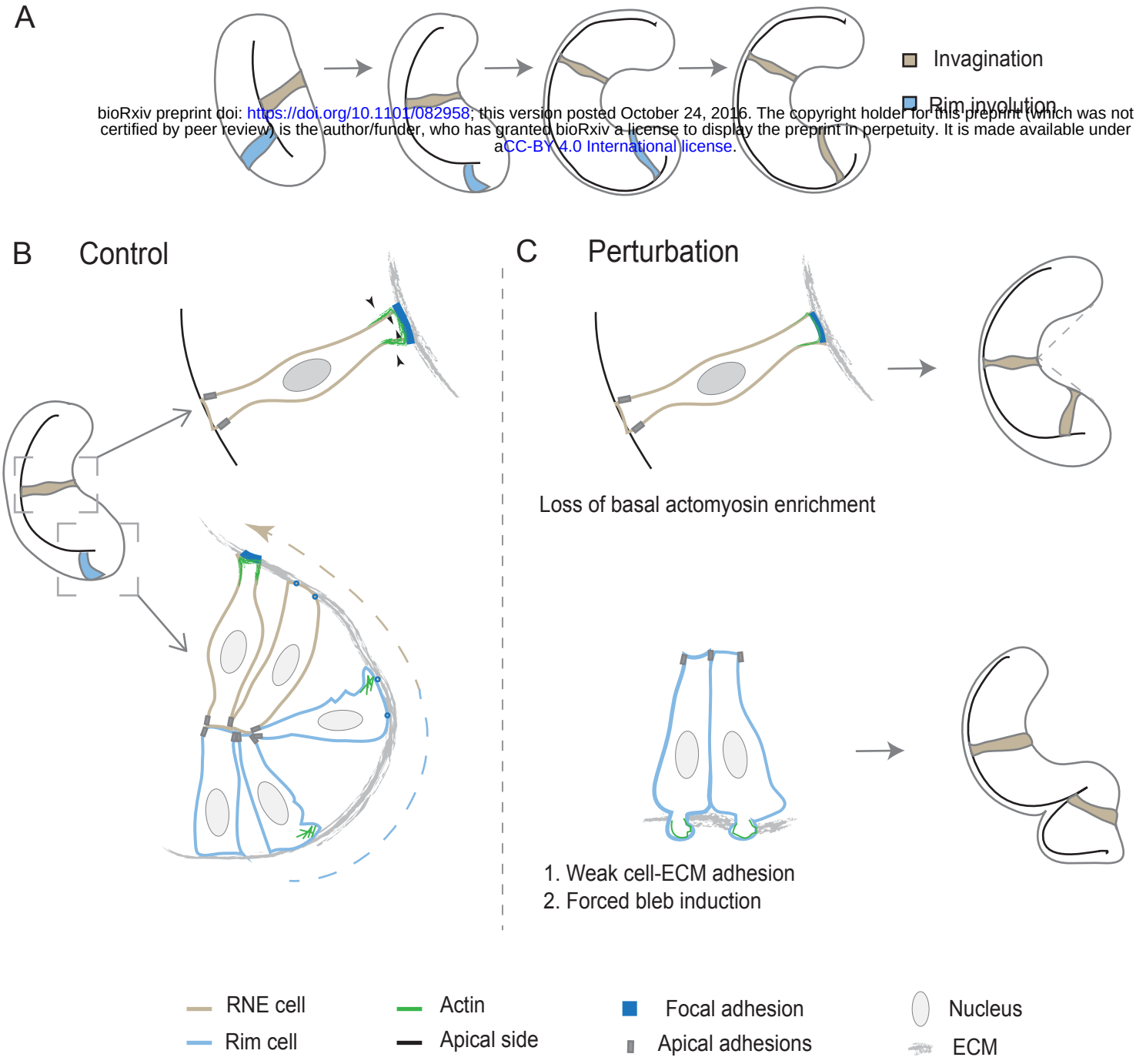

Figure 7: Concerted action of basal foot shrinkage and rim involution shapes the hemispheric RNE.

A) Schematic representation of RNE morphogenesis. The cells in the bilayered optic vesicle shape the RNE into a hemispheric cup. Central RNE cells (brown) contribute to invagination and prospective neuroepithelial cells (blue) undergo rim involution to reach the inner layer of the cup.
B) In control conditions, invagination is driven by basal foot shrinkage, basally enriched actomyosin-driven constriction and overall compaction by neighboring cells. Rim cells undergo active collective epithelial migration to reach the inner layer of the cup. Protrusive migratory dynamics of rim cells change to adherent behavior when cells reach the inner layer.
C) Loss of basal actomyosin enrichment leads to slowed invagination, which can result in a wider optic cup. Perturbation of migratory behavior causes severe defects in optic cup architecture, resulting in an S-shaped optic cup.

Supplemental experimental procedures:

Cloning strategies

The following constructs were generated using Gateway cloning system.

pCS2+ paxillin mKate2 : Middle entry clone for zebrafish paxillin was a kind gift from Clarissa Henry (Goody and Henry, 2010). It was combined with mKate2 pENTR(R2-L3) (kind gift from Andrew Oates, Crick Institute, London, UK) and pCS2 Dest(R1-R3) backbone (Villefranc et al., 2007).

pCS2+ Integrin beta1b-mKate2 : Zebrafish Integrin β1b (NM_001034987.1) was amplified from cDNA using the following primers to generate a middle entry clone without a stop codon at the end.

5' GGGGACAAGTTTGTACAAAAAAGCAGGCTGGatggacgtaaggctgctcc 3'

5' GGGGACCACTTTGTACAAGAAAGCTGGGTtttgccctcatatttagggttgac 3'

It was combined with mKate2 pENTR(R2-L3) (kind gift from Andrew Oates, Crick Institute, London, UK) and pCS2 Dest(R1-R3) backbone (Villefranc et al., 2007).

Hsp70::EGFP-Rac1T17N :

pcDNA3-EGFP-Rac1-T17N was a gift from Gary Bokoch (Addgene plasmid # 12982) (Subauste et al., 2000). To generate a middle entry clone EGFP-Rac-T17N was amplified using the following primers:

5' GGGGACAAGTTTGTACAAAAAAGCAGGCTGGatggtgagcaagggcgagg3'

5' GGGGACCACTTTGTACAAGAAAGCTGGGTttacaacagcaggcattttc 3'

It was combined with hsp70 promoter p5ENTR(L4-R1) (Kwan et al., 2011) and pTol2+pA_pDEST(R4-R2) (Villefranc et al., 2007).

Hsp70::mKate2-Rac1T17N :

pcDNA3-EGFP-Rac1-T17N was a gift from Gary Bokoch (Addgene plasmid # 12982) (Subauste et al., 2000). To generate a 3' entry clone Rac-T17N was amplified using the following primers:

5' GGGGACAGCTTTCTTGTACAAAGTGGCTatgcaggccatcaagtgtg 3'

5' GGGGACAACTTTGTATAATAAAGTTGCttacaacagcaggcattttctc 3'

It was combined with hsp70 promoter p5ENTR(L4-R1) (Kwan et al., 2011), mKate2 pENTR(L1-L2) (kind gift from Andrew Oates, Crick Institute, London, UK) and pTol2+pA_pDEST(R4-R3) (Villefranc et al., 2007).

Zebrafish transgenesis

1 nl of the mix of Tol2 plasmid Tol2-bactin::mKate2-ras (Icha et al., 2016) containing 20 ng/µl and Tol2 transposase RNA 30 ng/µl in ddH_2O was injected into the cytoplasm of one-cell stage embryos. F_0 embryos with observed fluorescence signal were grown to adulthood and Tg carriers were identified by outcross with wild type fish.

Western blot

For each condition protein sample from 5 embryos was used and western blot performed. Following antibodies dilutions were used: 1:500 anti-laminin (Sigma L-9393), 1:500 anti-phospho-ERM (Cell Signaling 3141), 1:10000 Anti-α-Tubulin (Sigma T6074), 1:20000 peroxidase conjugated anti-Mouse (Jackson Immuno 315-035-003), 1:20000 peroxidase conjugated anti-Rabbit (Jackson Immuno 111-035-003).

Integrin intensity analysis

Embryos were injected with Integrin-mKate2 RNA alone or mixed with Opo morpholino. Single optical sections featuring complete apico-basal length of RNE cells were imaged and chosen for analysis. Average integrin-mKate2 intensity was measured along a 20 pixel thick line marked along the apicobasal axis of RNE. An average was calculated along the line for 0-5μm (basal) and 25-30μm (central) region. A ratio of basal average intensity to central average intensity was calculated for each embryo. This was calculated for 5 different embryos each.

References

Goody, M.F., and Henry, C.A. (2010). Dynamic interactions between cells and their extracellular matrix mediate embryonic development. Mol. Reprod. Dev. *77*, 475–488.

Icha, J., Grunert, C., Rocha-Martins, M., and Norden, C.(2016). Independent modes of ganglion cell translocation ensure correct lamination of the zebrafish retina bioRxiv, 066761

Kwan, K.M., Otsuna, H., Kidokoro, H., Carney, K.R., Saijoh, Y., and Chien, C.B. (2011). A complex choreography of cell movements shapes the vertebrate eye. Development *139*, 359–372.

Subauste, M.C., Herrath, Von, M., Benard, V., Chamberlain, C.E., Chuang, T.H., Chu, K., Bokoch, G.M., and Hahn, K.M. (2000). Rho family proteins modulate rapid apoptosis induced by cytotoxic T lymphocytes and Fas. J Biol Chem *275*, 9725–9733.

Villefranc, J.A., Amigo, J., and Lawson, N.D. (2007). Gateway compatible vectors for analysis of gene function in the zebrafish. Dev Dyn *236*, 3077–3087.

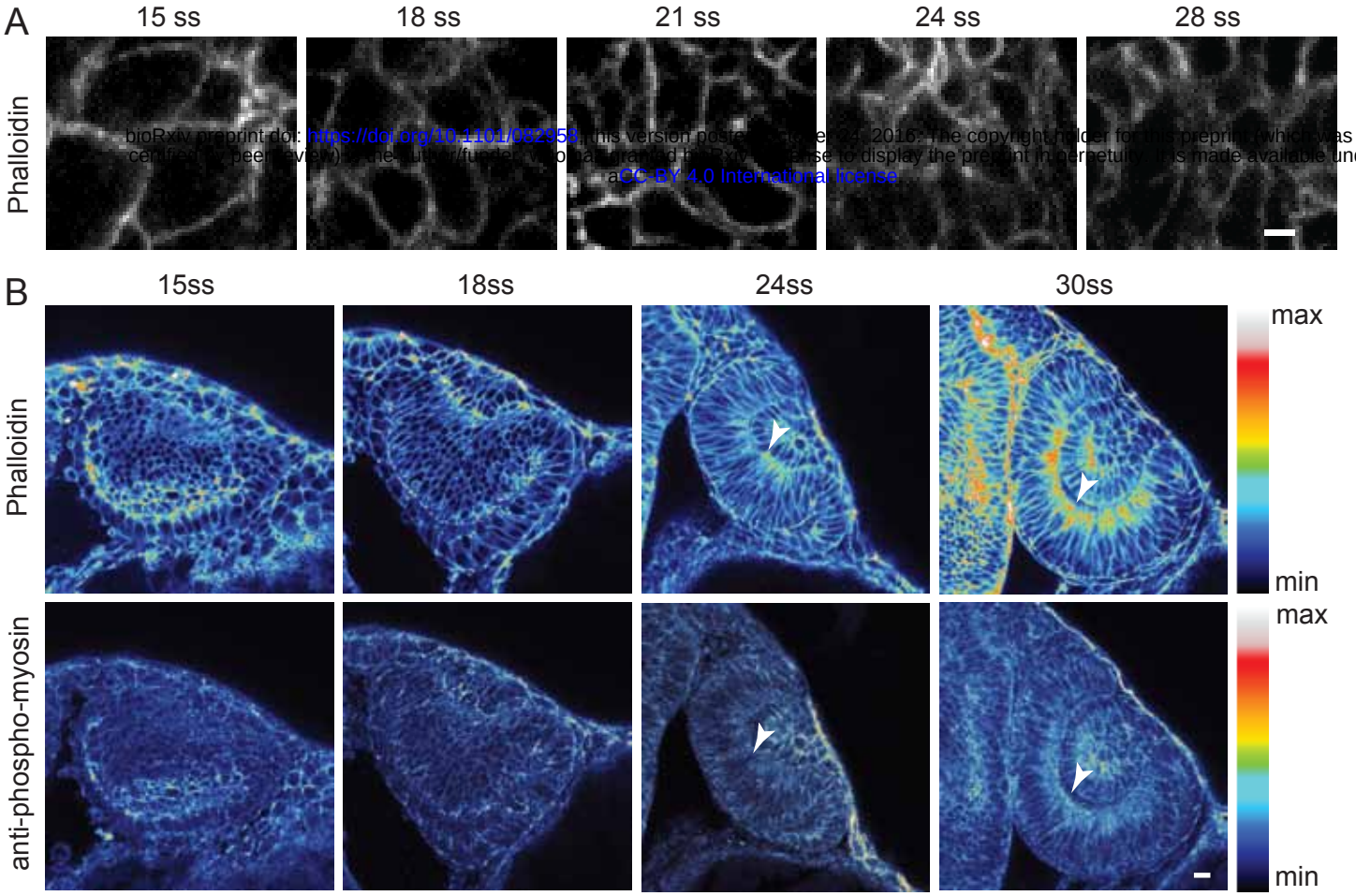

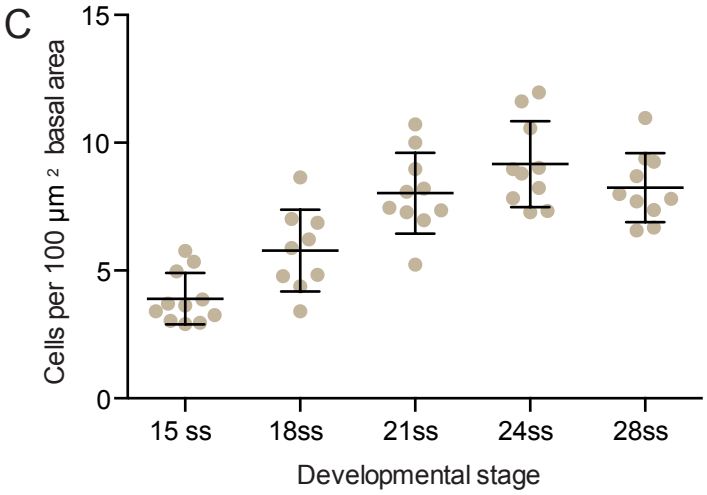

Figure S1, Related to Figure 1.

A) Confocal scans of the basal side of the RNE cells stained with phalloidin at different developmental stages. Scale bar=2 µm.

B) Confocal scans of different stages of RNE morphogenesis stained for phalloidin and phosphomyosin. Arrowheads point at basal enrichment. Lookup table indicates the minimum and maximum intensity values. Scale bar=10 µm.

C) Average number of cells per 100 µm² basal area of RNE at different stages of development. Mean±SD, n=10 embryos each.

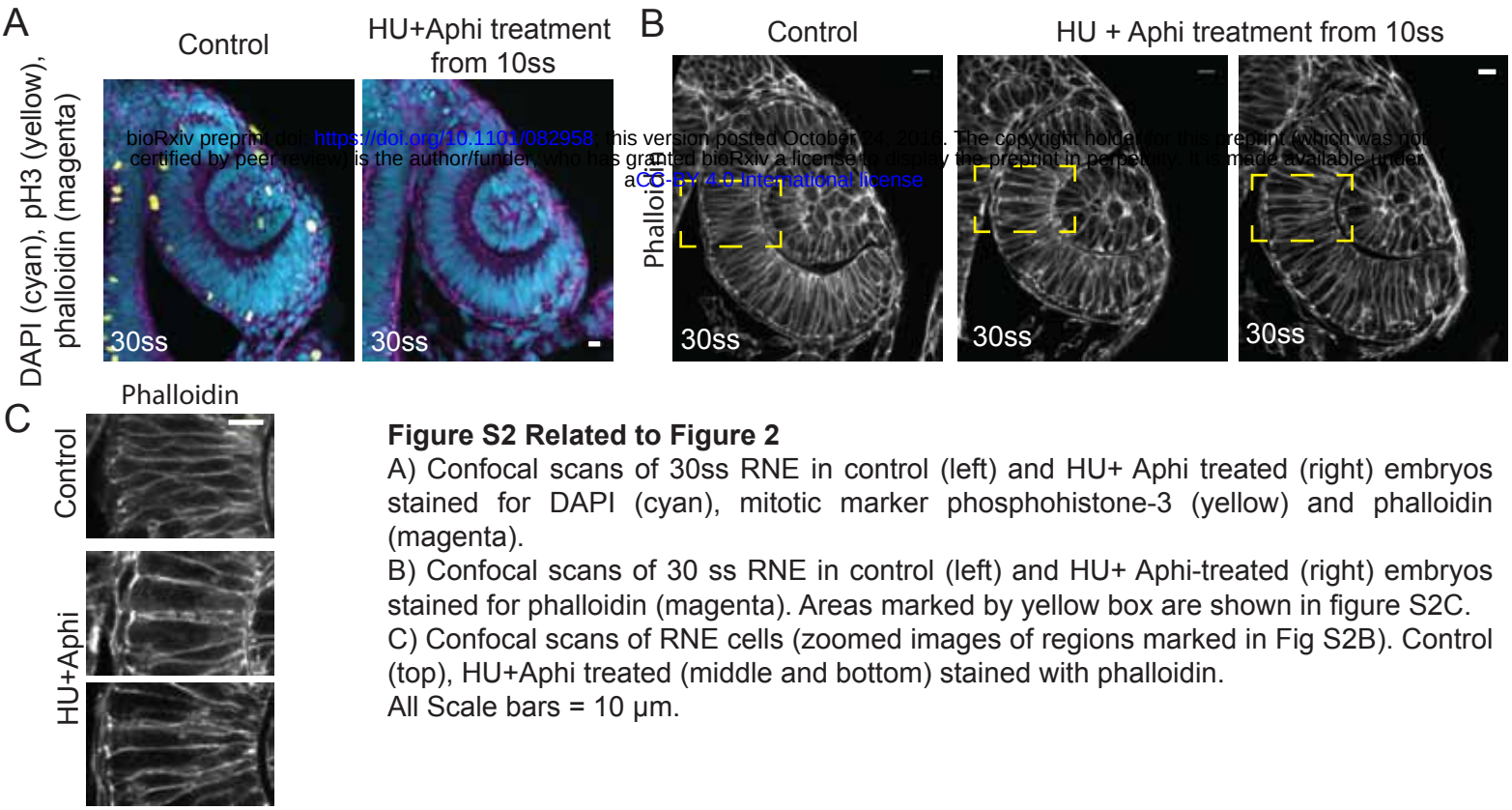

Figure S2 Related to Figure 2

A) Confocal scans of 30ss RNE in control (left) and HU+ Aphi treated (right) embryos stained for DAPI (cyan), mitotic marker phosphohistone-3 (yellow) and phalloidin (magenta).

B) Confocal scans of 30 ss RNE in control (left) and HU+ Aphi-treated (right) embryos stained for phalloidin (magenta). Areas marked by yellow box are shown in figure S2C.

C) Confocal scans of RNE cells (zoomed images of regions marked in Fig S2B). Control (top), HU+Aphi treated (middle and bottom) stained with phalloidin.

All Scale bars = 10 μm.

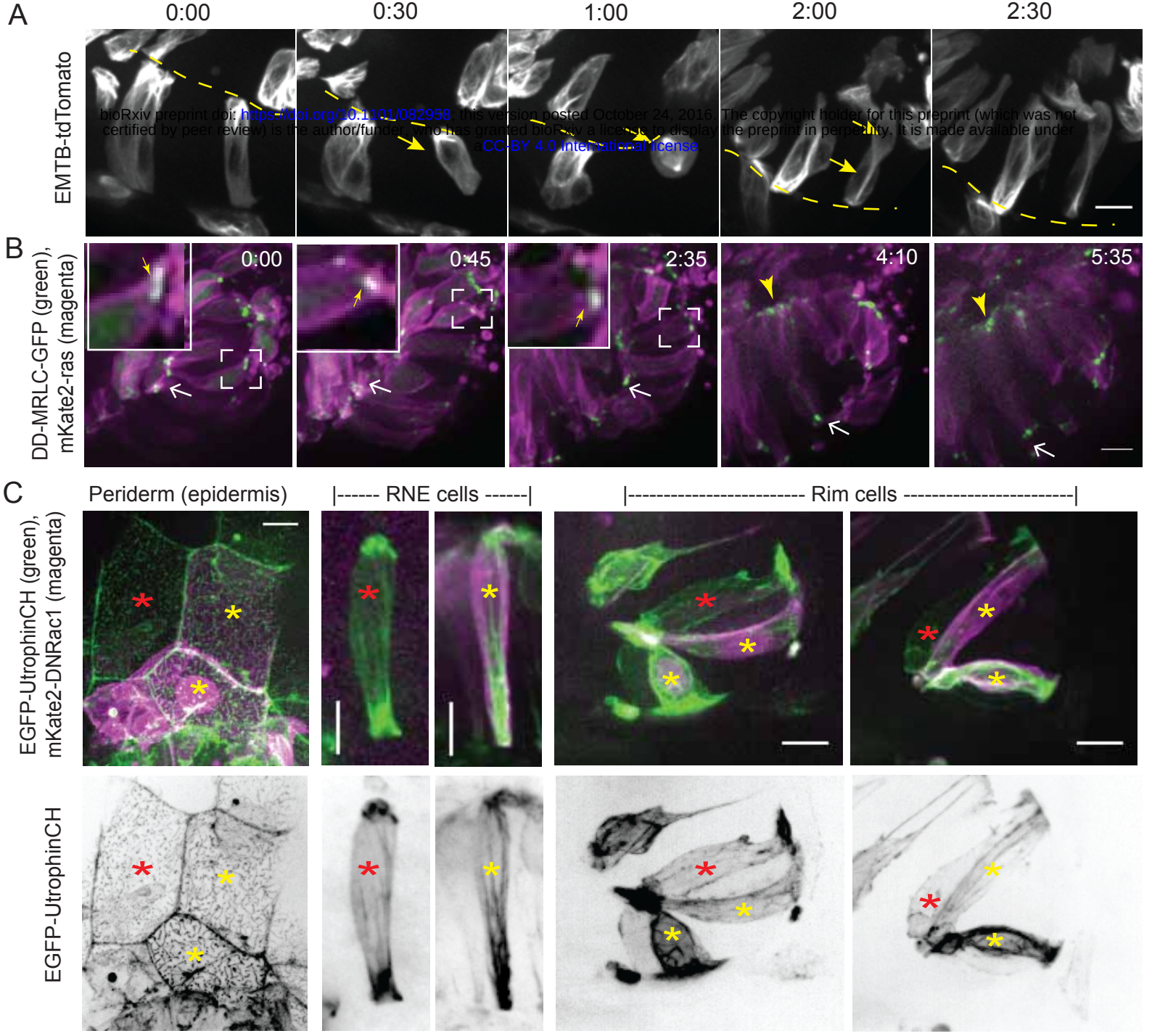

Figure S3- Related to Figure 3

A) Time-lapse imaging of rim zone with mosaic expression of EMTB-tdTomato. Arrows mark the cell dividing during rim involution. Dashed line marks the apical side. Imaging started at 17-18ss.

B) Time-lapse imaging of rim zone with mosaic expression of myl12.1-GFP and mKate2-ras. Inlays show zoomed marked area. Yellow arrows indicate basal myosin punctae in the rim cells. White arrows mark adherens junctions. Arrowheads mark basally enriched stable myosin pool in the RNE. Imaging started at 15-16 ss.

C) Confocal scans of F-actin distribution marked by heatshock induced EGFP-Utrophin in peridermal cells of the epidermis (left) , RNE cells (middle) and rim cells (right). Yellow asterisk marks cells expressing heatshock induced mKate-DN-Rac. Red asterisk marks control cells. Note that upon DN-Rac expression, the pattern of actin microridges is affected in the epidermis and actin organisation shows filamentous arrangement in the RNE and rim cells.

Scale bars=10µm, Time h:min.

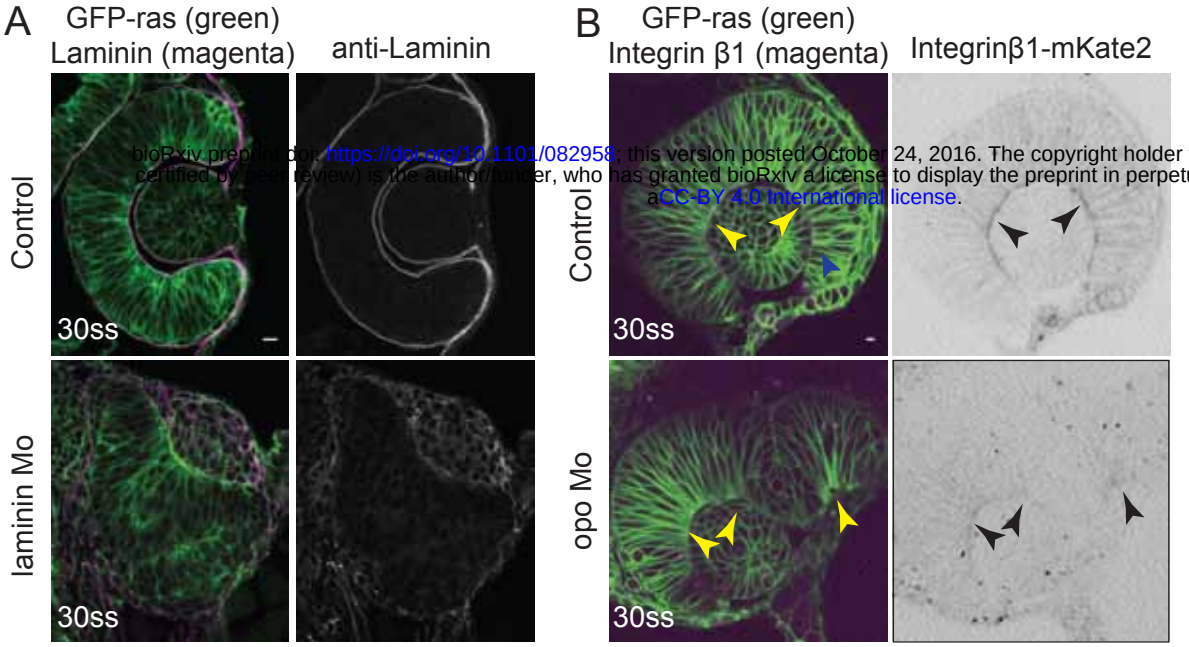

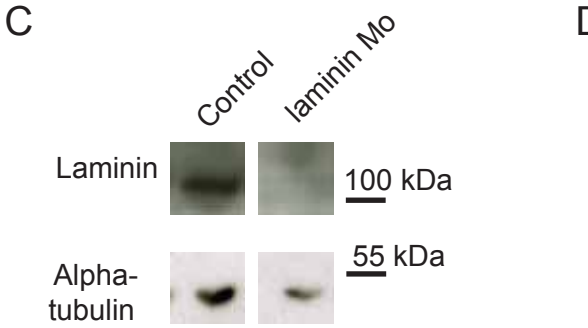

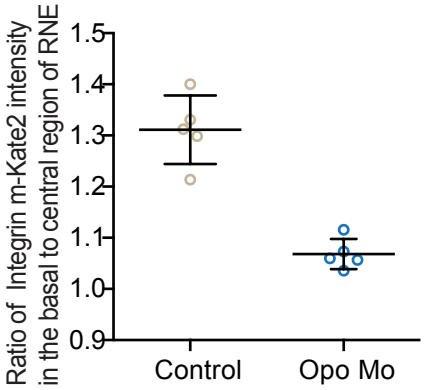

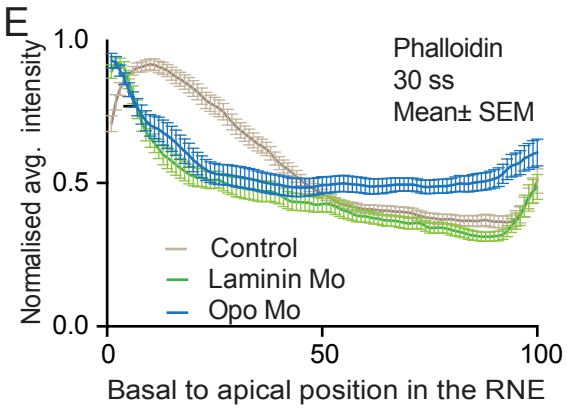

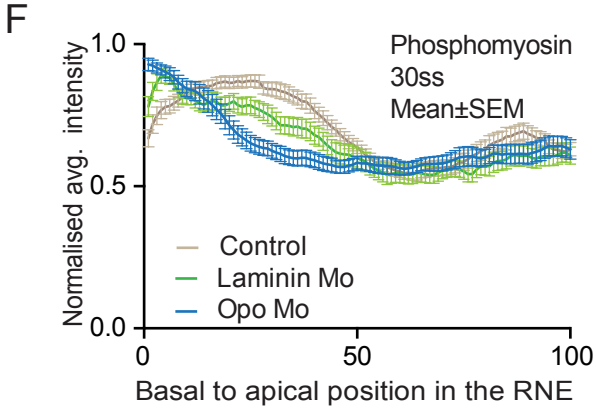

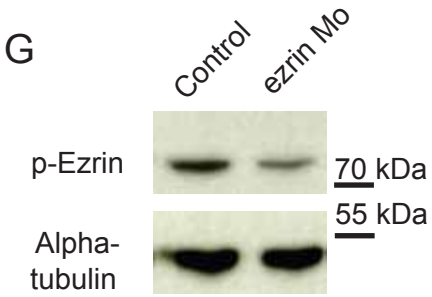

Figure S5, Related to Figure 4 and 5.

A) Confocal scan of 30ss RNE in control (top) and laminin morphants (bottom) marked with GFP-ras stained for laminin. Morphant shows S-shaped RNE and reduced laminin staining. Scale bar=10 μm.

B) Confocal scan of side view of 30ss RNE in GFP-ras and Integrin-β1-mKate2 RNA injected control (top) and opo morphant (bottom). Morphant shows S-shaped RNE with secondary invagination zone and highly reduced basal localization of integrin. Scale bar=10 μm.

C)Western blot for laminin and alpha tubulin in control and laminin morphant.

D) Ratio of average integrin β1-mKate2 signal at the basal to central region in the RNE in optical section along the apicobasal axis of the RNE at 30 ss. Mean±SD, n=5 embroys.

E,F) Normalized average intensity distributions of phalloidin (E) and phosphomyosin (F) in tissue volume along the apicobasal axis of the RNE at 30 ss. Mean±SEM. Control (brown) n=25, laminin Mo (green) n=19 and Opo Mo (blue) n=20. Tissue sections (n); embryos, N=5.

G) Western blot for p-Ezrin and alpha tubulin in control ans ezrin morphant.

H) Brightfield image of Ezrin morphant embryo at 30ss stage.